

# Journal of Geophysical Research: Atmospheres

## RESEARCH ARTICLE

10.1002/2016JD025168

### Key Points:

- Turbulence effects on a heavy precipitation case are investigated using the WRF-bin model
- Spatial distribution of surface precipitation amount is altered due to the turbulence effects
- Enhanced upward water vapor transportation due to the turbulence effects is the key for microphysical changes

### Correspondence to:

J.-J. Baik,  
jjbaik@snu.ac.kr

### Citation:

Lee, H., and J.-J. Baik (2016), Effects of turbulence-induced collision enhancement on heavy precipitation: The 21 September 2010 case over the Korean Peninsula, *J. Geophys. Res. Atmos.*, 121, 12,319–12,342, doi:10.1002/2016JD025168.

Received 31 MAR 2016

Accepted 4 OCT 2016

Accepted article online 7 OCT 2016

Published online 25 OCT 2016

## Effects of turbulence-induced collision enhancement on heavy precipitation: The 21 September 2010 case over the Korean Peninsula

Hyunho Lee<sup>1</sup> and Jong-Jin Baik<sup>1</sup>

<sup>1</sup>School of Earth and Environmental Sciences, Seoul National University, Seoul, South Korea

**Abstract** The effects of turbulence-induced collision enhancement (TICE) on a heavy precipitation event that occurred on 21 September 2010 over the middle Korean Peninsula are examined. For this purpose, an updated bin microphysics scheme incorporating TICE for drop-drop and drop-graupel collisions is implemented into the Weather Research and Forecasting (WRF) model. The numerical simulation shows some differences in the strong precipitation system compared to the observations but generally captures well the important features of observed synoptic conditions, surface precipitation, and radar reflectivity. While the change in domain-averaged surface precipitation amount due to TICE is small and similar to that due to small initial perturbations, the spatial distribution of surface precipitation amount is somewhat altered due to TICE. The surface precipitation amount is increased due to TICE in the area where the largest surface precipitation occurred, but the effects of different flow realizations also contribute to the changes. TICE accelerates the coalescence between small cloud droplets, which induces a decrease in condensation and an increase in excess water vapor transported upward. This causes an increase in relative humidity with respect to ice at high altitudes, hence increasing the depositional growth of ice particles. Therefore, the ice mass increases due to TICE, and this increase induces the increases in riming and melting of ice particles. A series of these microphysical changes due to TICE are regarded as partially contributing to the increase in surface precipitation amount in some areas, hence inducing alterations in the spatial distribution of surface precipitation amount.

### 1. Introduction

For many decades, it has been hypothesized that in-cloud turbulence increases the collision rate between cloud particles compared to the calculated collision rate considering only motions induced by gravity. Starting from the pioneering work done by *Saffman and Turner* [1956], many numerical methods have been used to estimate turbulence-induced collision enhancement. Recently, with increased available computing power, more precise calculation becomes possible using direct numerical simulation (DNS) models or turbulent statistical models. For spherical drop-drop collisions, several studies [e.g., *Zhou et al.*, 2001; *Franklin et al.*, 2005; *Ayala et al.*, 2008; *Wang et al.*, 2008; *Kunnen et al.*, 2013] presented enhanced collision rates using DNS models and *Pinsky et al.* [2008] also presented the similar conclusions using a turbulent statistical model. Regarding ice particles, *Pinsky et al.* [1998] presented enhanced collision rates between drop and graupel by assuming spherical graupel particles. For nonspherical cloud particles, although very few studies have focused on this subject, *Siewert et al.* [2014] provided a framework and preliminary results on turbulence-induced collision enhancement for the collisions of prolate and oblate ellipsoids.

Previous studies have reported that turbulence can increase the collision rate by up to several times compared to the gravitational collision rate [e.g., *Grabowski and Wang*, 2013]. Therefore, it is reasonable to expect that such an increase in collision rate would alter cloud development and precipitation. Following this expectation, using numerical models that include a cloud microphysics scheme, the effects of turbulence-induced collision enhancement on cloud development and precipitation have been examined for the last decade. *Franklin* [2008] improved the autoconversion rate in a bulk microphysics scheme by considering turbulence-induced enhancement rate and demonstrated faster raindrop formation due to turbulence. Using a large-eddy simulation (LES) model coupled with a bulk microphysics scheme, *Seifert et al.* [2010] showed an increase in surface precipitation from shallow cumuli due to turbulence. *Wyszogrodzki et al.* [2013] and *Grabowski et al.* [2015], using an LES model coupled with a bin microphysics scheme, also showed an increase in surface precipitation from shallow cumuli and suggested that the increase in surface

precipitation mainly comes from dynamical feedback (i.e., the increased cloud top height). *Franklin* [2014] suggested that dynamical feedback depends on cloud types. Although almost all previous studies have shown an increase in surface precipitation from shallow cumuli, *Lee et al.* [2015] showed that turbulence can decrease the surface precipitation from shallow cumuli in clean and highly humid environmental conditions due to decreased condensation.

Compared to studies on shallow warm clouds, there are relatively a few studies that investigate turbulence effects on mixed-phase deep convective clouds. *Benmoshe et al.* [2012] performed a series of numerical simulations with different aerosol concentrations using a bin microphysics cloud model and demonstrated that the effects of turbulence appear to be opposite to the effects of increased aerosols in an isolated mixed-phase deep convective cloud. *Benmoshe and Khain* [2014] extended the results of *Benmoshe et al.* [2012] and showed that the effects of turbulence on accumulated precipitation are not very significant, but the effects of turbulence on microphysical structures are comparatively large. *Lee et al.* [2014] suggested that the turbulence effect on precipitation from mixed-phase deep convective clouds differ with vertical wind shear: the difference is clearer in the uniform basic-state wind condition than in the sheared basic-state wind condition.

However, to the best of the authors' knowledge, the previous studies that are concerned with turbulence effects on mixed-phase deep convective clouds have dealt with idealized environmental conditions, and there is no study that examines turbulence effects through real-case simulations. Therefore, we implement a state-of-the-art bin microphysics scheme into a mesoscale numerical model and investigate turbulence effects on a heavy precipitation case that occurred over the Korean Peninsula. The numerical model used in this study, synoptic conditions of the case, and experimental setup are described in section 2. Simulation results are presented and discussed in section 3. A summary and conclusions are given in section 4.

## 2. Method

### 2.1. Model Description

The Weather Research and Forecasting (WRF) model version 3.6.1 is used in this study [Skamarock et al., 2008]. To investigate the effects of turbulence on the heavy precipitation case, we have implemented the updated version of bin microphysics scheme of the Hebrew University Cloud Model (HUCM) [Khain et al., 2011] into the WRF model. This bin microphysics scheme considers seven hydrometeors (liquid drop, plate-, column-, and dendrite-shape ice crystal, snow, graupel, and hail) and takes activation, vapor diffusional processes (condensation, evaporation, deposition, and sublimation), collision, secondary ice multiplication, breakup, freezing, and melting processes into consideration. The scheme divides the entire mass range of hydrometeors into 43 mass doubling bins and predicts the number concentration of each bin. The mass range considered in the scheme is the same for all hydrometeors ( $3.35 \times 10^{-14} \text{ kg}$ – $1.47 \times 10^{-1} \text{ kg}$ ). The smallest drop radius is  $2 \mu\text{m}$ , and by using the 43 mass doubling bins, the scheme can consider very large hail particle, whose radius is up to  $3.39 \text{ cm}$ . The number concentration of aerosol particles is also predicted using 43 mass doubling bins in which the largest aerosol particle radius is  $2 \mu\text{m}$ .

In addition to the number concentration of each bin of each hydrometeor, this updated version of HUCM predicts the rimed fraction of snow and the liquid water fractions of snow, graupel, and hail. In the model, it is regarded that a snow particle consists of aggregated, rimed, and liquid parts and that the increased mass due to collection with a supercooled drop becomes rimed mass. The rimed mass and liquid water mass as well as the particle mass are advected and diffused as a scalar in the WRF model. The rimed fraction of snow (the ratio of rimed mass to the total mass of a snow particle) is used to update the density and terminal velocity of snow particles at every time step and every grid point [Khain et al., 2011], assuming that the rimed part of the snow particle has the same properties as those of a hail particle. As the rimed fraction of a snow particle increases, the characteristics of the particle become similar to those of graupel or hail. The type conversion from snow to graupel or hail is considered using the rimed fraction of snow, which is the same as in *Khain et al.* [2011] and *Iguchi et al.* [2014].

The liquid water fractions of snow, graupel, and hail are used to calculate a time-dependent gradual melting process [Phillips et al., 2007]. The effects of liquid water fractions were discussed in *Phillips et al.* [2007] and

**Table 1.** TICE for Drop-Graupel When the Turbulence Dissipation Rate is 400 (800)  $\text{cm}^2 \text{s}^{-3}$ 

Drop Radius ( $\mu\text{m}$ )	Graupel Radius ( $\mu\text{m}$ )							
	30	100	300	500	700	1000	2000	3000
10	4.0 (6.0)	4.5 (7.5)	2.8 (4.5)	2.3 (3.5)	2.0 (3.0)	1.75 (2.4)	1.35 (1.67)	1.17 (1.3)
20	2.6 (4.8)	4.65 (7.65)	2.85 (4.75)	2.35 (3.65)	2.0 (3.1)	1.87 (2.5)	1.6 (1.75)	1.3 (1.35)
50	2.7 (4.5)	4.5 (7.5)	3.1 (5.25)	2.55 (4.17)	2.2 (3.5)	2.12 (2.9)	1.7 (2.0)	1.4 (1.7)
80	2.25 (3.5)	2.0 (5.0)	2.5 (4.5)	2.1 (3.8)	2.3 (3.4)	2.19 (2.85)	1.7 (2.15)	1.44 (1.7)
100	1.0 (1.5)	1.35 (4.0)	1.3 (3.75)	1.3 (3.4)	1.2 (3.15)	1.28 (2.75)	1.25 (2.19)	1.12 (1.7)
200	1.0 (1.4)	1.0 (2.0)	1.1 (2.0)	1.1 (2.0)	1.1 (1.9)	1.0 (1.83)	1.0 (1.67)	1.0 (1.4)
300	1.0 (1.2)	1.0 (1.3)	1.0 (1.4)	1.0 (1.3)	1.0 (1.3)	1.0 (1.3)	1.0 (1.28)	1.0 (1.25)

Iguchi *et al.* [2014]. It is noted that the melting process needs to be further improved to consider relatively large vertical grid sizes more properly. For snow, both the rimed fraction and the liquid water fraction are calculated even when the temperature is above 0°C. The rimed fraction and aggregated fraction of snow are calculated using

$$\begin{aligned} f_a &= 1 - f_r, \\ f'_r &= (1 - f'_l)f_r, \\ f'_a &= (1 - f'_l)(1 - f_r). \end{aligned} \quad (1)$$

Here  $f_a$  and  $f_r$  are the aggregated fraction and the rimed fraction of snow before melting, respectively, and  $f'_r$ ,  $f'_l$ , and  $f'_a$  are the rimed fraction, liquid water fraction, and aggregated fraction of snow after melting, respectively. Following (1), the ratio between the rimed fraction and aggregated fraction is assumed to remain the same before and after the melting process (i.e.,  $f_a/f_r = f'_a/f'_r$ ).

All aerosol particles are treated as a scalar: they are advected and diffused in the model. The aerosol particles whose radii are larger than a critical radius are activated into cloud condensation nuclei (CCN). The Köhler equation [Köhler, 1936] is used to calculate the critical aerosol radius for a given grid-scale supersaturation. To consider the formation of ice nuclei in the model, deposition and condensation-freezing nucleation in Meyers *et al.* [1992], immersion freezing in Bigg [1953] and Vali [1975], and secondary ice crystal formation in Hallett and Mossop [1974] are included. Scavenging of aerosols by precipitation is not considered in this model.

The results of Pinsky *et al.* [2008] and Pinsky *et al.* [1998] are used to consider the turbulence-induced collision enhancement (TICE) of drop-drop collision and drop-graupel collision, respectively. TICE of drop-drop collision uses the turbulence dissipation rate and Taylor microscale Reynolds number as measures of turbulence intensity. The turbulent kinetic energy (TKE) and buoyancy frequency are used to obtain the turbulence dissipation rate and Taylor microscale Reynolds number. There are 11 precalculated lookup tables following the given pairs of turbulence dissipation rate and Taylor microscale Reynolds number. The ranges of turbulence dissipation rates and Taylor microscale Reynolds numbers considered in this study are  $10 \text{ cm}^2 \text{s}^{-3}$ – $1000 \text{ cm}^2 \text{s}^{-3}$  and 5000–20000, respectively. TKE is calculated using the Mellor-Yamada-Janjic (MYJ) scheme [Janjic, 2002] in the WRF model. Descriptions of the procedure for calculating TKE in the MYJ scheme and the procedure for calculating turbulence dissipation rate and Taylor microscale Reynolds number from TKE and buoyancy frequency are given in Appendix A.

It is noted that while Pinsky *et al.* [2008] adopted a theoretical approach and a turbulence statistical model to evaluate TICE, some studies have been conducted to evaluate TICE using DNS models [e.g., Ayala *et al.*, 2008; Wang *et al.*, 2008]. There have been comparisons between them, and recent studies [e.g., Grabowski and Wang, 2013] show that TICE from the different studies becomes similar to each other.

TICE of drop-graupel collision uses only the turbulence dissipation rate. There are two precalculated tables in which the turbulence dissipation rates are  $400 \text{ cm}^2 \text{s}^{-3}$  and  $800 \text{ cm}^2 \text{s}^{-3}$  (Table 1), and interpolation/extrapolation methods are used to obtain TICE of drop-graupel collision, which is the same as in Benmoshe and Khain [2014] and Lee *et al.* [2014] and also similar to the methods used in Seifert *et al.* [2010], Wyszogrodzki *et al.* [2013], and Franklin [2014].

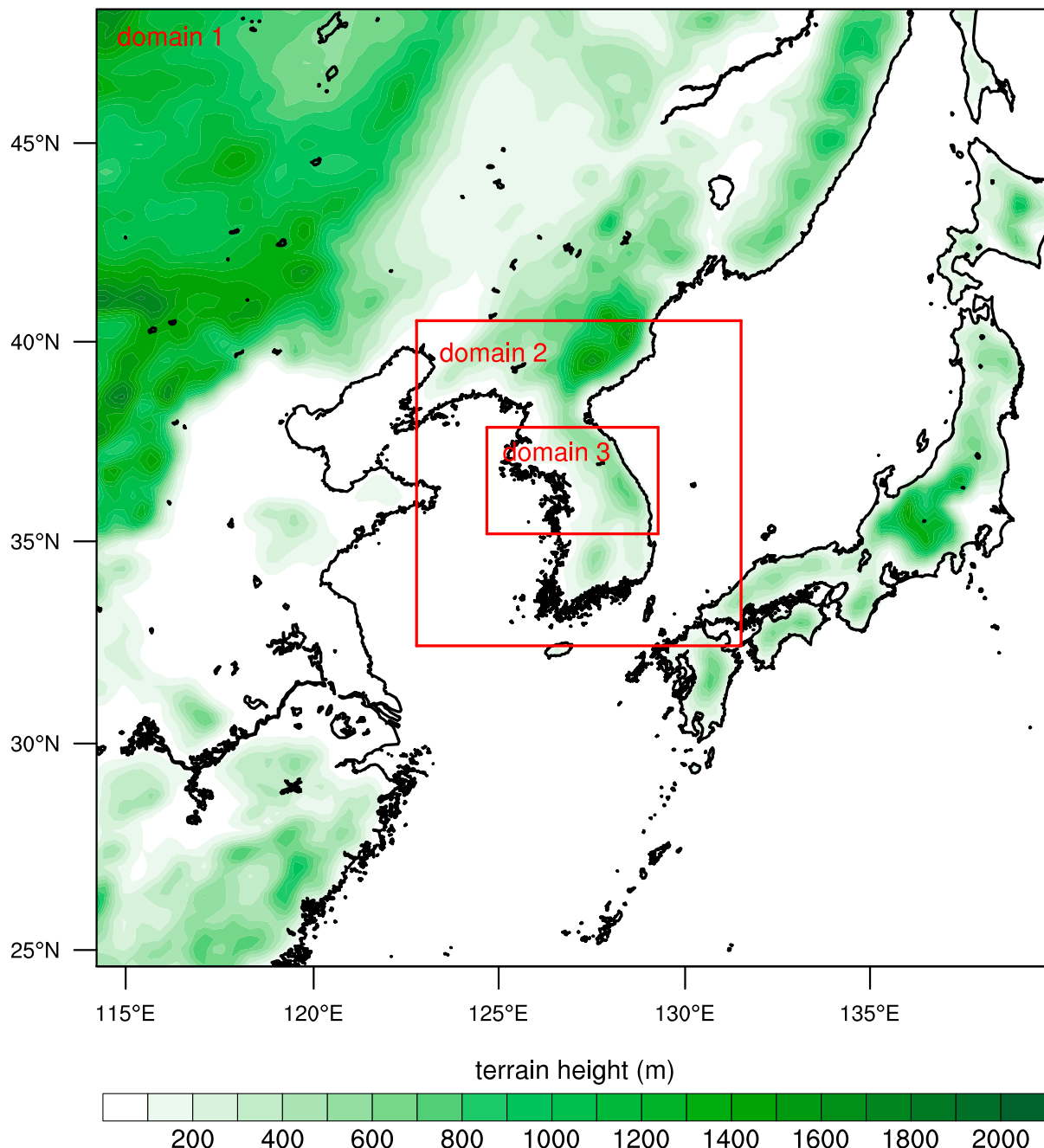


**Figure 1.** Illustration of three nested model domains with terrain height.

## 2.2. Precipitation Case

A heavy precipitation event occurred on 21 September 2010 over the middle Korean Peninsula. The maximum 24 h accumulated precipitation amount recorded by the Automatic Weather Station (AWS) operated by the Korea Meteorological Administration is 293 mm. The surface precipitation was concentrated over a relatively short period (approximately 4–5 h), and the maximum precipitation rate reached as high as  $100 \text{ mm h}^{-1}$ . Thermodynamic conditions for this case were somewhat different from typical heavy precipitation conditions: convective available potential energy was almost zero around the heavy precipitation area during the precipitation period. Instead, synoptic conditions were the key to the production of this heavy precipitation. A tropical depression transported abundant water vapor from the south, and two

**Table 2.** Model Domain Configuration and List of Physics Schemes in the WRF Model Used in This Study

	Domain 1	Domain 2	Domain 3
Horizontal grid size	25 km	5 km	1.667 km
Horizontal grid number	108 × 108	181 × 181	286 × 178
PBL	Mellor-Yamada-Janjic ( <i>Janjic</i> [2002])		
Subgrid-scale cumulus	Kain-Fritsch ( <i>Kain</i> [2004])		none
Shortwave radiation		MM5 ( <i>Dudhia</i> [1989])	
Longwave radiation		RRTM ( <i>Mlawer et al.</i> [1997])	
Land surface		Noah ( <i>Chen and Dudhia</i> [2001])	
Surface layer		Eta similarity ( <i>Janjic</i> [2002])	

different high pressure systems made a convergence zone near the middle Korean Peninsula. The transported water vapor was supplied to the convergence zone, and the heavy precipitation occurred in the convergence zone. A detailed description of the synoptic and mesoscale conditions of this event was provided in *Jung and Lee* [2013].

### 2.3. Experimental Setup

The model domain configuration and selected physics schemes are shown in Figure 1 and Table 2. Three domains are used with one-way nesting, with horizontal grid sizes of 25, 5, and 1.667 km, respectively. NCEP (National Centers for Environmental Prediction) final analysis data ( $1^\circ \times 1^\circ$ , 6 h intervals) are used to provide initial and boundary conditions at the outermost domain. The model top is 50 hPa, which is approximately 20 km. The number of vertical layers is 33, and the vertical grid size is ~30 m in the lowest layer and increases up to ~800 m with height. Model integrations are performed for 24 h, from 12 UTC 20 September to 12 UTC 21 September (from 21 local standard time (LST) 20 September to 21 LST 21 September), and the first 6 h is regarded as model spin-up time.

The initial aerosol size distribution is set to follow the Twomey equation [Twomey, 1959], which is the same as that of *Khain et al.* [2000] and *Lee et al.* [2014]. The initial aerosol number concentration is set for the CCN number concentration at 1% supersaturation to be  $100 \text{ cm}^{-3}$  below  $z=2 \text{ km}$  and decreases exponentially above  $z=2 \text{ km}$  with an e-folding depth of 2 km. The aerosol replenishment scheme provided in *Jiang and Wang* [2014] is employed:

$$\left. \frac{\partial N_a}{\partial t} \right|_{\text{repl}} = \frac{N_{a0} - N_a}{\tau}, \quad (2)$$

where  $N_a$  is the aerosol number concentration,  $N_{a0}$  is the initial aerosol number concentration, and  $\tau$  is the relaxation time (1 h in this study). This aerosol replenishment scheme is used to restore the aerosol concentration to the value at the initial state. It is noted that in the simulation results of this study, the maximum cloud droplet number concentration, which is mainly controlled by the initial aerosol number concentration, is  $83 \text{ cm}^{-3}$ . This value is somewhat small from the point that the area of interest is mostly land, although some studies also report the maximum cloud droplet number concentration similar to that of this study [e.g., *Jiang et al.*, 2016]. In future studies, more proper treatments of aerosol number concentration and aerosol-related physical processes would be helpful.

## 3. Results and Discussion

### 3.1. Validation

First of all, the synoptic-scale weather patterns, which are one of the keys to this heavy precipitation event, are compared from the observation and simulation. Figure 2 shows the observed weather chart at 850 hPa level and the corresponding model initial data at 21 LST 20 September, and the observed weather chart at 850 hPa level and the corresponding model simulation result at 09 LST 21 September. The synoptic-scale weather conditions shown in the charts were in favor of a typical heavy precipitation event over the Korean Peninsula. From 21 LST 20 September to 09 LST 21 September, cold air had moved from the

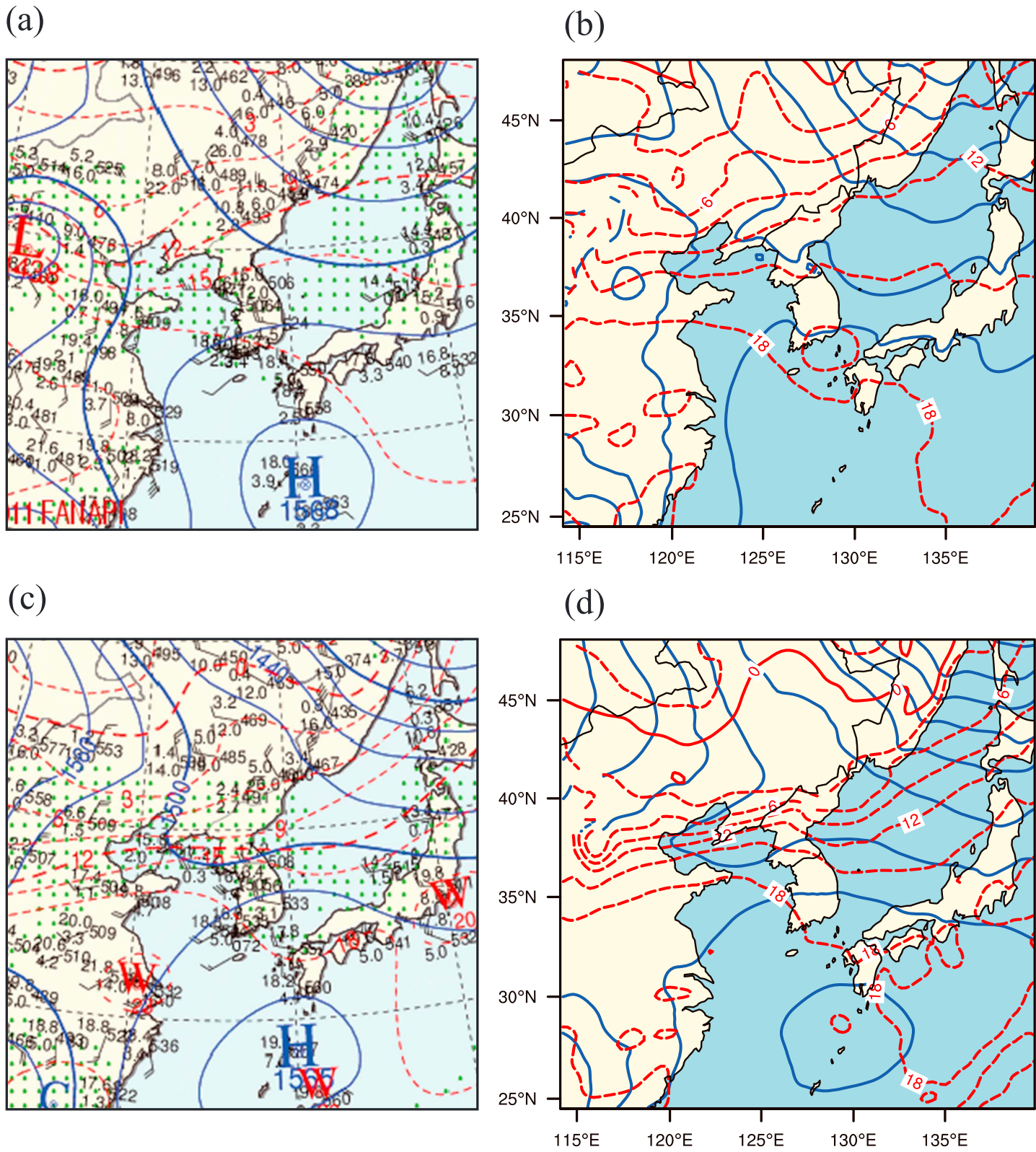


**Figure 2.** Synoptic weather charts at 850 hPa level (a) provided by the Korea Meteorological Administration and (b) depicted using NCEP final analysis data at 21 LST 20 September 2010. Intervals for geopotential height (blue solid line) and isotherm (red dashed line) are 30 m and 3°C, respectively. In Figure 2b, the 0°C isotherm line is represented by the red solid line. (c) The same as Figure 2a but at 09 LST 21 September 2010. (d) The same as Figure 2b but simulated at 09 LST 21 September 2010.

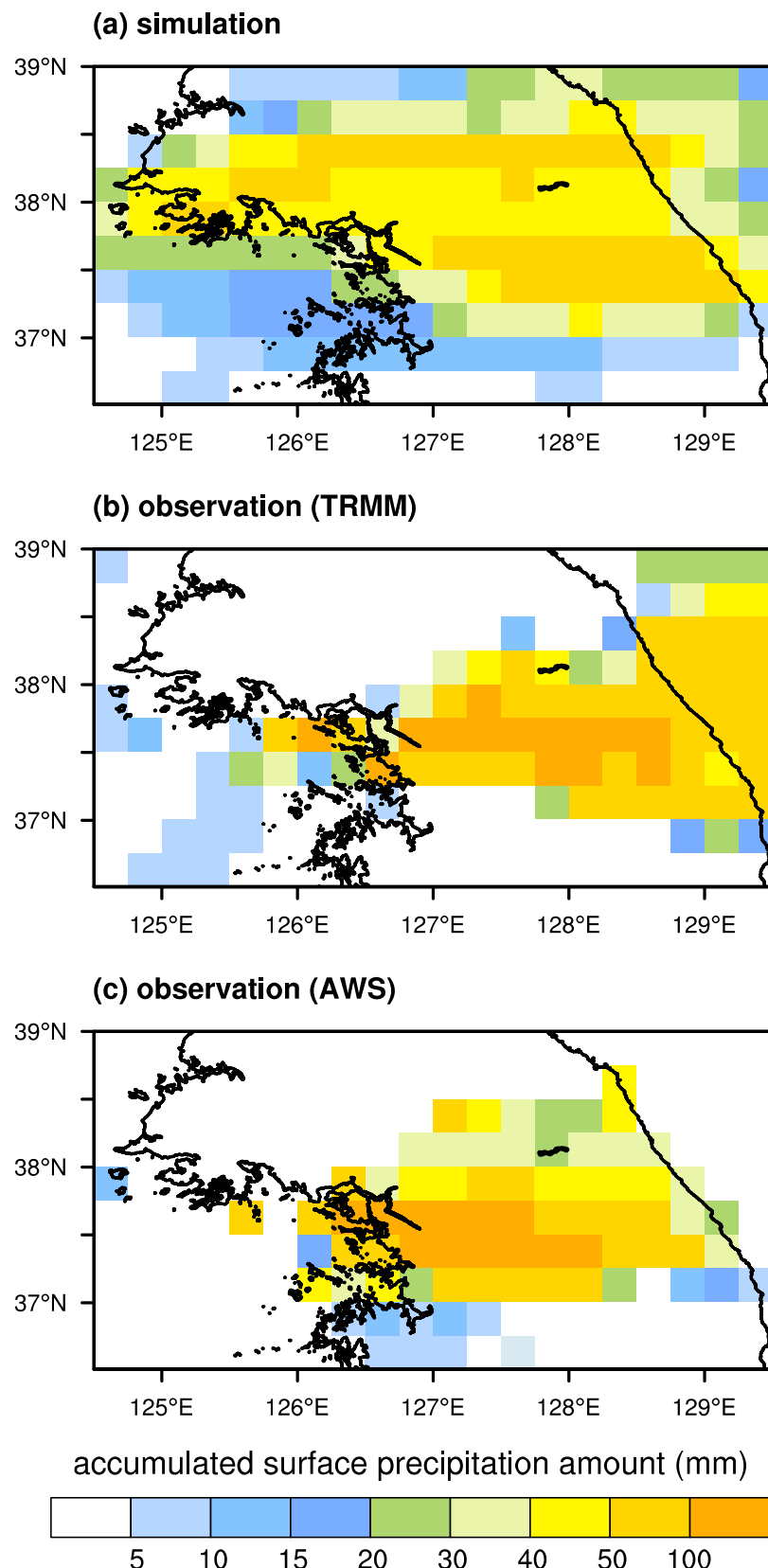


**Figure 3.** Surface precipitation amount accumulated over 03–21 LST 21 September (a) in the simulation case with TICE, (b) in the observation by TRMM, and (c) in the observation by AWSs operated by the Korea Meteorological Administration.

northwest of the Korean Peninsula (see isotherms for 0°C (the slightly thick red line) or 3°C in Figures 2a and 2c) while warm air was almost stationary (see 15°C or 18°C isotherms (the red lines crossing the Korean Peninsula) in the same figures). Therefore, a narrow zone with a high temperature gradient formed, where a mesoscale convective system can be easily developed with promoting frontogenesis [e.g., Bluestein, 1993]. Moreover, a tropical depression was on southern China at 21 LST 20 September, which provided a plenty of water vapor in the zone through southwesterly winds along the North Pacific high. The features mentioned above are well simulated in the WRF model (Figure 2d). Although the zone with a high temperature gradient in the simulation is slightly deflected to the north compared to that in the observation, the important features of the weather system that caused the heavy precipitation event, which are the movements of the isotherms and the tropical depression, are well reproduced in the simulation.

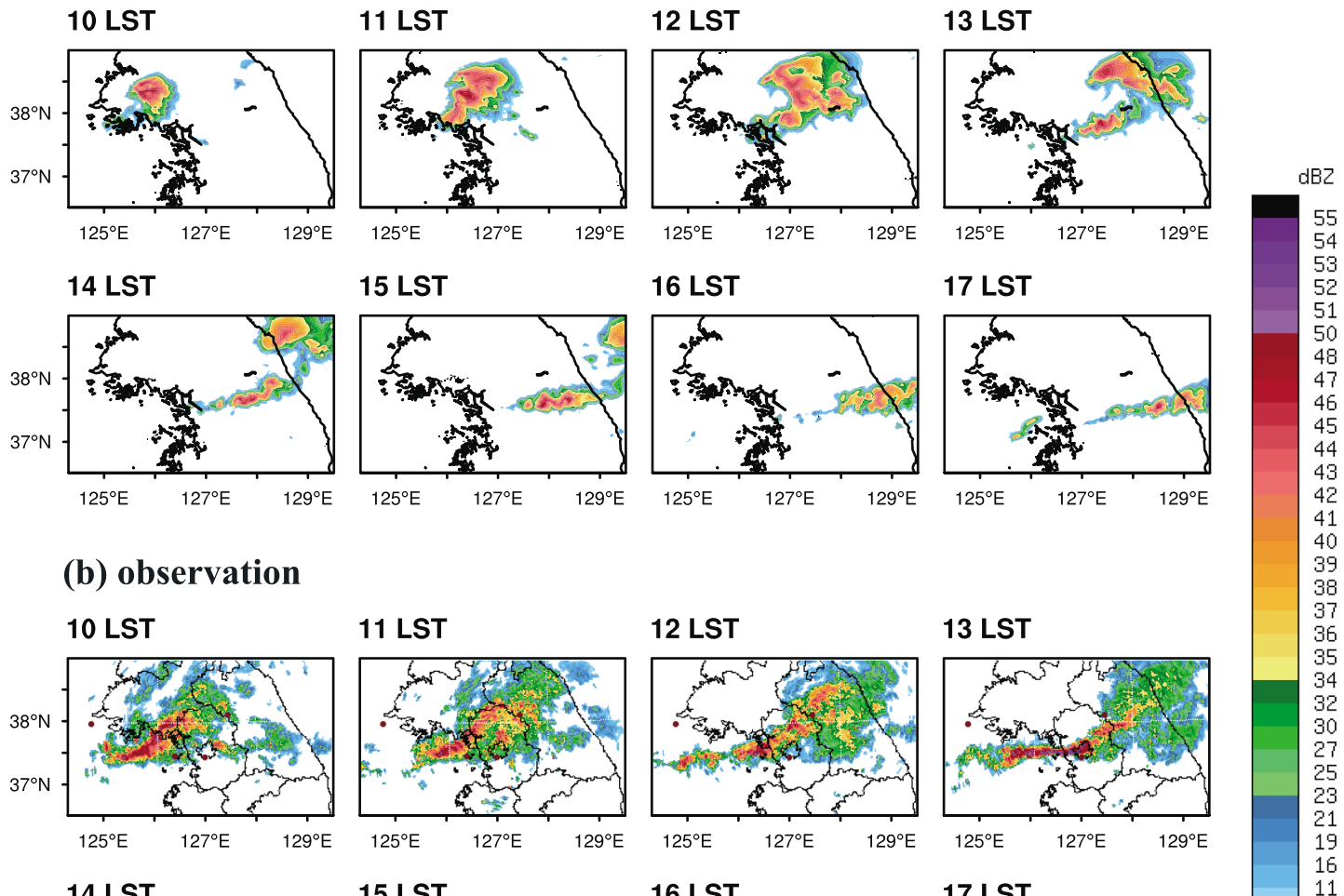
The fields of surface precipitation amount accumulated over 03–21 LST simulated in this study and observed by the Tropical Rainfall Measuring Mission (TRMM) [Huffman *et al.*, 2007] and by the automatic weather stations (AWSs) operated by the Korea Meteorological Administration are plotted in Figure 3. Note that the AWS observation covers only South Korea, which is south of ~38°N in Figure 3. For easier comparison, the AWS data are gridded in the same resolution as the TRMM data by averaging observation values at AWSs within each grid area in the TRMM data. Compared to the TRMM and AWS observations, the model tends to underestimate the surface precipitation amount in Seoul and its nearby area (near the center of the domain), where the largest surface precipitation amount was observed, and the simulated surface precipitation is spread over a larger area. However, the simulated surface precipitation is generally similar to the TRMM and AWS observations in that the strong band-type precipitation is concentrated in the middle Korean Peninsula and the spatial deviation of surface precipitation amount is large.

The time evolution of radar reflectivity fields for 10–17 LST from the simulation and observation is shown in Figure 4. The Rayleigh scattering is applied to each bin of drop, snow, graupel, and hail to calculate the radar reflectivity. In the observed radar reflectivity, strong precipitation echoes are seen in the northwest of Seoul (depicted by a closed curve near the center of each figure in Figure 4b) at 10 LST. While a part of the strong precipitation echoes move from the northwest to the northeast of Seoul, other narrow and strong (>40 dBZ) band-type precipitation echoes stay Seoul and its nearby area for approximately 4–5 h, from 13 LST to 17–18 LST. In Seoul and its nearby area, the simulated radar reflectivity shows somewhat underestimated reflectivity compared to the observed radar reflectivity. In addition, in the north of Seoul, the simulated radar reflectivity is delayed and shifted to the north compared to the observed radar reflectivity. However, the general features in the observed radar reflectivity, such as the two separated echoes and the narrow and strong band-type precipitation echoes in Seoul and its nearby area, are well reproduced in the simulation.

### 3.2. Turbulence Effects on Precipitation

By including and excluding TICE, the effects of turbulence on cloud development are investigated focusing on the surface precipitation. First, it is examined whether the turbulence structure is well simulated. Figure 5 shows the time series and vertical profiles of the maximum turbulence dissipation rate in the cases with and without TICE. The time series of the maximum turbulence dissipation rate show that strong turbulence appears intermittently, particularly in the cloud developing stage (07–13 LST). The maximum turbulence dissipation rate during this period reaches approximately  $2000 \text{ cm}^2 \text{ s}^{-3}$  in the case with TICE, which is in the simulated ranges in *Benmoshe and Khain* [2014] and *Lee et al.* [2014] that numerically investigated an isolated deep convective cloud using a two-dimensional model with finer grid resolutions. The vertical distributions of the maximum turbulence dissipation rate show that strong turbulence dissipation rates mainly appear at high altitudes ( $z > 7 \text{ km}$ ), which is also in good agreement with the result of *Benmoshe and Khain* [2014]. Therefore, although the grid size in this study is somewhat large (1.667 km in the horizontal, ~0.8 km in the vertical), particularly for a detailed investigation of the turbulence structure in the clouds, the simulated turbulence intensity is similar to that of the studies using higher spatial resolutions so the effects of turbulence on a real precipitation case can be examined using the present experimental settings. However, it would be better to compare the results to those from 3-D cloud simulations with finer grid sizes, although it is hard to be realized at this stage due to the limited computing resources. It is noted that the turbulence intensity is generally stronger in the case with TICE than in the case without TICE, which is possibly due to increased latent heating in the case with TICE mainly caused by increased deposition and riming that will be discussed later (Figure 14) [*Benmoshe and Khain*, 2014].

## (a) simulation



## (b) observation

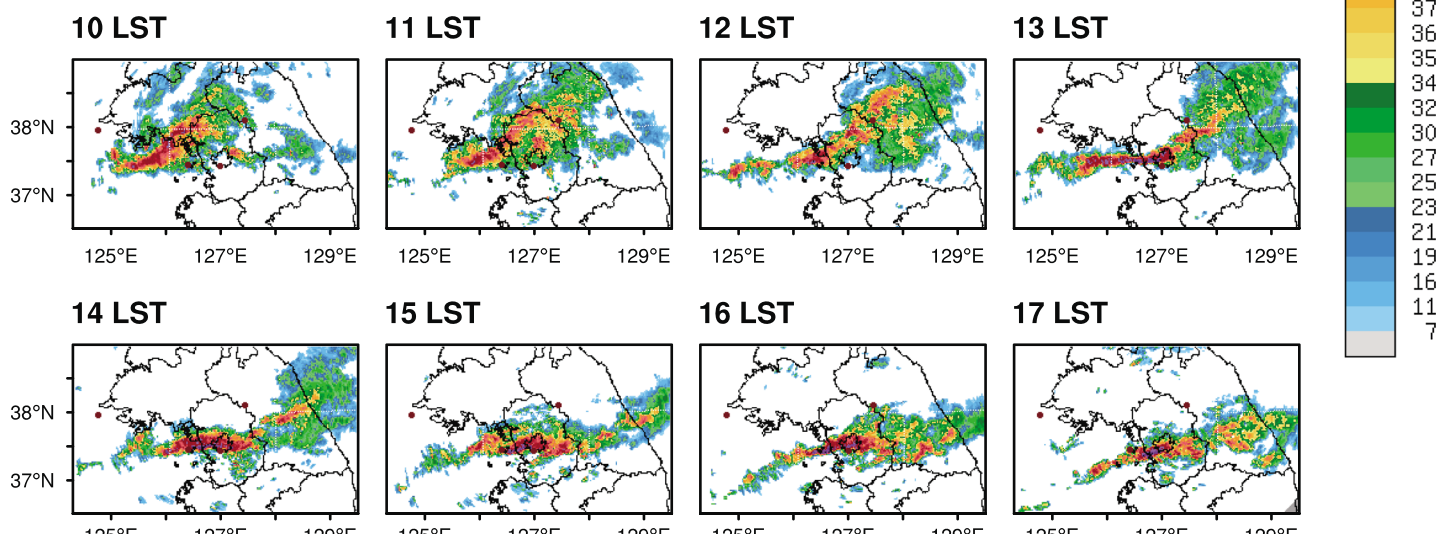


**Figure 4.** Fields of radar reflectivity (Constant Altitude Plan Position Indicator at  $z = 1.5$  km) for 10–17 LST 21 September (a) in the simulation case with TICE and (b) in the observation by radars operated by the Korea Meteorological Administration. Seoul is depicted in Figure 4b with a small closed curve near the center of each figure ( $\sim 37.5^\circ\text{N}$ ,  $\sim 127^\circ\text{E}$ ). Red dots in Figure 4b correspond to the radar observation sites.

The fields of surface precipitation amount accumulated over 03–21 LST in the cases with and without TICE are shown in Figures 6a and 6b. The overall amount of surface precipitation is not significantly altered due to TICE, mainly because the total precipitation amount of the domain is largely controlled by humidity and stability of the air. The overall spatial distributions are generally similar to each other, but the field of difference in accumulated surface precipitation amount between the two cases shows that there are spatial shifts in surface precipitation due to TICE (Figure 6c). Precipitation in the northern part of the domain (north of  $\sim 37.5^\circ\text{N}$ ) is largely shifted to northwest, and precipitation in the southern part of the domain (south of  $\sim 37.5^\circ\text{N}$ ) shows a complex shift pattern. When Seoul and its nearby area, where the largest surface precipitation amount was observed (indicated as area A, see Figure 3), is focused, the surface precipitation amount

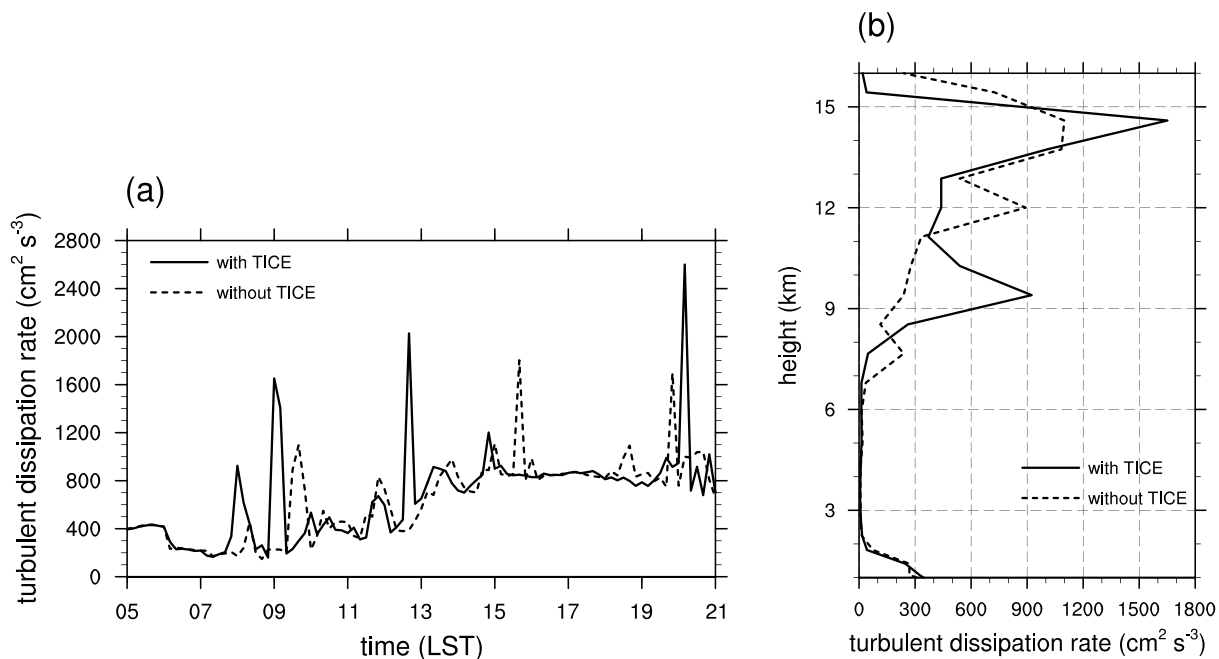


**Figure 5.** (a) Time series of the maximum turbulence dissipation rate in the clouds and (b) vertical profiles of the maximum turbulence dissipation rate in the clouds averaged over 07–13 LST in the cases with and without TICE. Cloudy point is defined using a total hydrometeor content threshold of  $0.01 \text{ g kg}^{-1}$ .

is larger in the case with TICE than in the case without TICE, although the shifts in precipitation would also contribute to the increase in precipitation in this area.

It is arguable whether the changes in results are causal due to TICE or coincidental due to different flow realizations. To distinguish between physical effects and coincidental effects, it would be better if an ensemble of simulations were performed. Recently, Grabowski [2014, 2015] suggested a piggybacking analysis that provides a rigorous extraction of the effects of different flow realizations from the changes in results due to the changes in model setup under idealized environmental conditions. However, up to now, it is hard to make an ensemble due to the limitation of computing resources. It is also hard to apply the piggybacking analysis to this study mainly due to the complex environmental conditions.

Instead of an ensemble, an additional experiment is conducted using perturbed initial conditions to examine the impacts of nonlinearity on the precipitation, although one additional experiment is still limited for examining the impacts clearly. In this experiment, the initial potential temperature at every grid point of the outermost domain is perturbed by random noise that is uniformly distributed between ( $-0.3 \text{ K}$  and  $0.3 \text{ K}$ ). TICE is not included in this experiment. Figure 6d shows the difference in accumulated surface precipitation amount between the case with TICE and the case without TICE but with the perturbed initial conditions. Compared to Figure 6c, although some local differences appear, the main characteristics are still observed: the large northwestward shift of precipitation in the northern part of the domain and the complex shift pattern in the southern part of the domain. In area A, the accumulated surface precipitation amount is still larger in the case with TICE than in the case without TICE but with the perturbed initial conditions. However, the increase is smaller than that obtained by comparing to the case without the perturbed initial conditions. It can be deduced that the TICE and different flow realizations together contribute to the increase in precipitation in area A.

The time series and the probability density function of accumulated surface precipitation amount for 03–21 LST averaged over the domain and area A are shown in Figure 7. The TICE-induced increase in surface precipitation amount averaged over the domain is as small as a few percent, and the increase due to TICE is similar in terms of scale to that due to the perturbed initial conditions. The probabilities for the accumulated surface precipitation amount of  $40\text{--}60 \text{ mm}$  and  $>80 \text{ mm}$  in the domain are increased due to TICE. However, the overall changes are small, and the change in probability for the accumulated

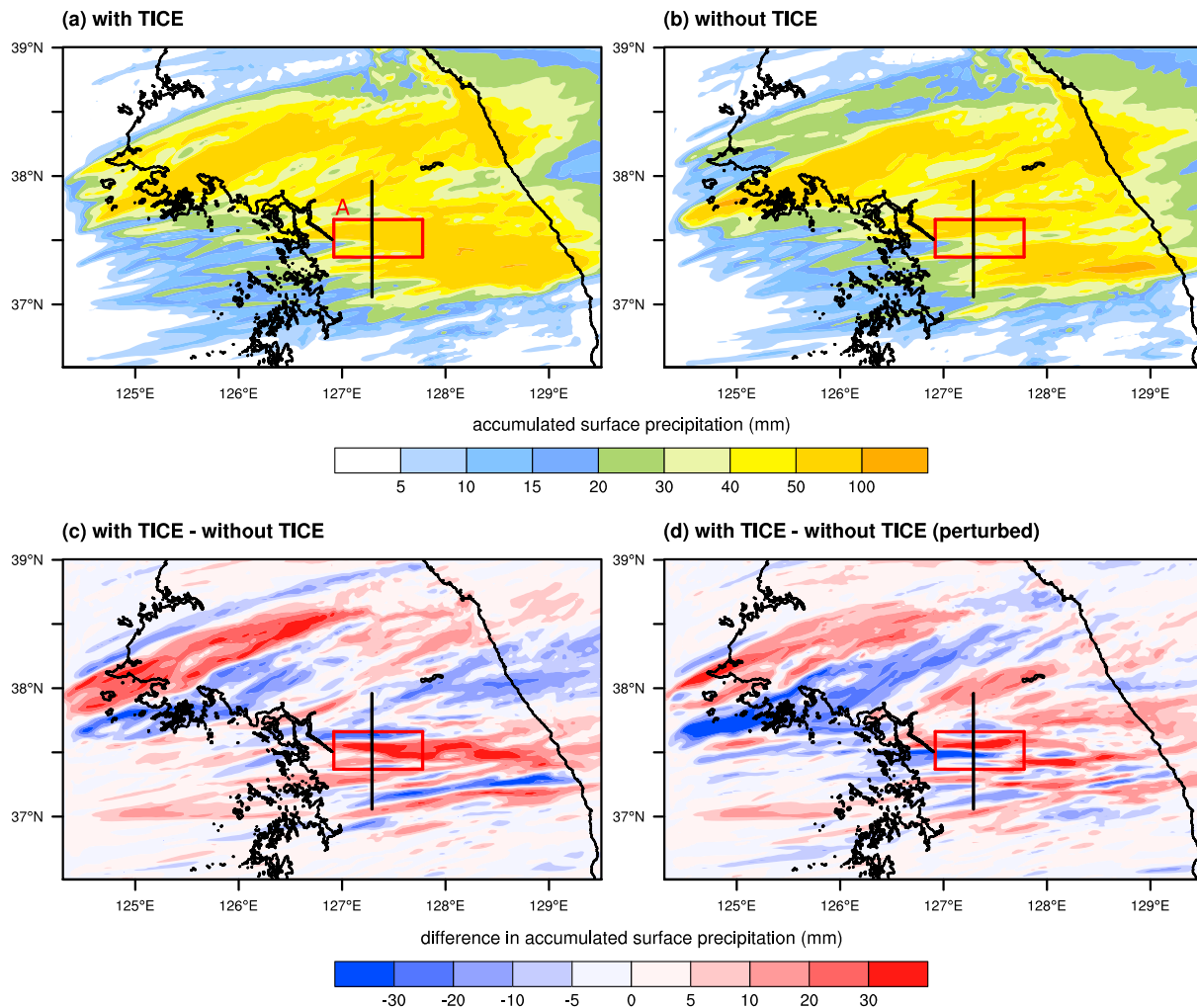


**Figure 6.** Surface precipitation amount accumulated over 03–21 LST in the cases (a) with TICE and (b) without TICE. (c) Difference in accumulated surface precipitation amount between the cases with and without TICE. (d) As in Figure 6c but for the cases with TICE and without TICE but with the perturbed initial conditions. The red rectangle indicates the area of interest.

surface precipitation amount of 60–80 mm due to TICE is not consistent. Thus, the effects of TICE in the domain are not statistically significant at least in a view of surface precipitation amount.

The increase in surface precipitation due to TICE is more distinct in area A than in the domain. In addition, the accumulated surface precipitation amount averaged over area A in the case with TICE is closer to the observation than that in the case without TICE. The maximum surface precipitation rate averaged over area A is ~30% larger in the case with TICE than in the case without TICE, and the accumulated surface precipitation amount is also ~10–20% larger in the case with TICE than in the case without TICE regardless of the initial conditions. The probabilities for the accumulated surface precipitation amount of 60–80 mm and >80 mm in area A are higher in the case with TICE than in the case without TICE. The effects of TICE on surface precipitation in area A become small when they are examined by comparing to the case without TICE but with the perturbed initial conditions, but the effects are shown to be still consistent. It is noted that when the effects of TICE on surface precipitation are examined in the area that includes area A but is extended approximately 4 times area A, the same trends (increase in averaged accumulated surface precipitation amount and increase in probability for large accumulated surface precipitation amount) are still observed (not shown).

However, it is not still definitive whether the changes in the simulation results in area A are causal or coincidental, mainly due to the limit number of conducted simulations. Although there seem to be systematic

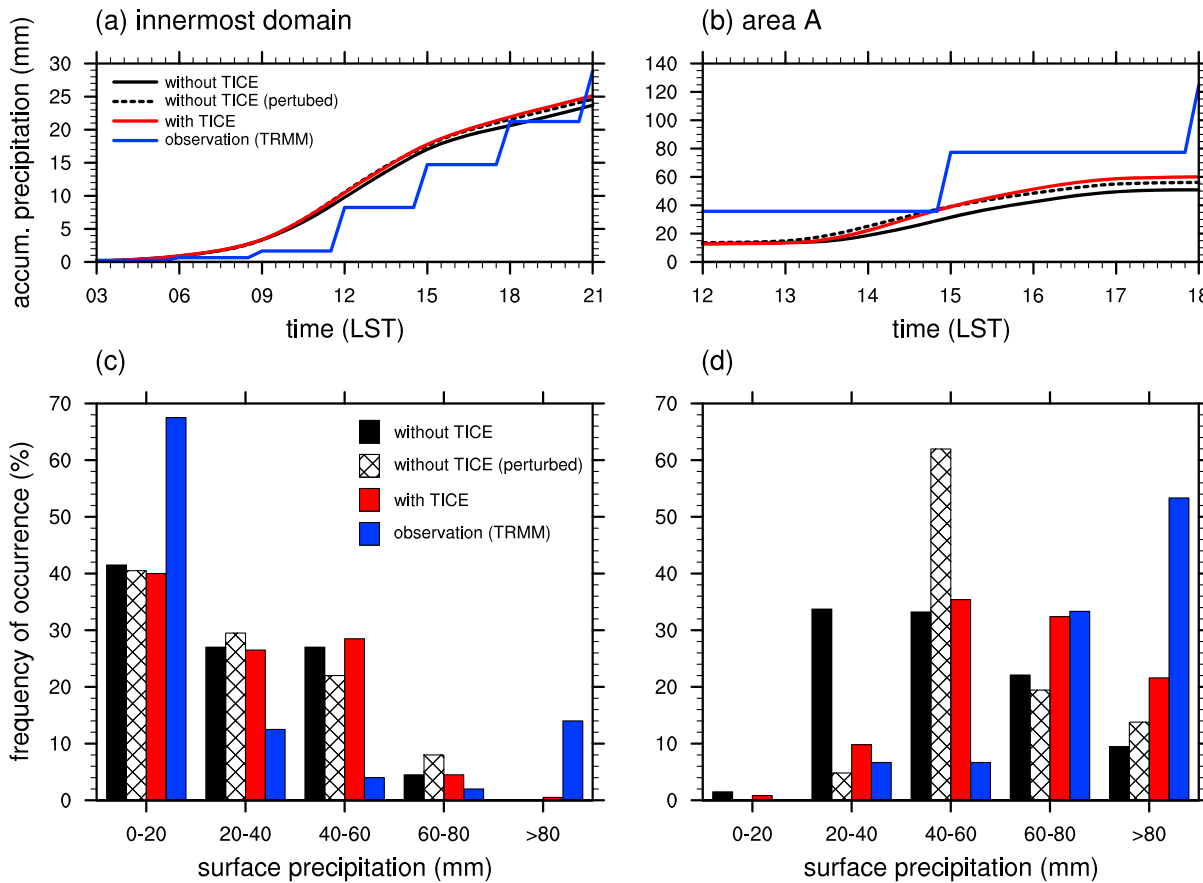


**Figure 7.** Time series of accumulated surface precipitation amount averaged over (a) the domain and (b) area A, and the probability density function of accumulated surface precipitation amount over (c) the domain and (d) area A in the cases with TICE, without TICE, and without TICE but with the perturbed initial conditions and in the observation using TRMM. It is noted that the temporal resolution of TRMM is 3 h.

differences in surface precipitation due to TICE in area A, the effects of TICE shown in the simulations are definitely a mixture of the physical effects of TICE and the effect of different flow realizations. Further in-depth studies that carefully distinguish between coincidental effects and physical effects are needed to clarify the effects of turbulence on cloud development and precipitation.

### 3.3. Turbulence Effects on Cloud Microphysical Structures

Cloud microphysical structures are analyzed to examine the effects of TICE on cloud development. Figure 8 shows the vertical profiles of each hydrometeor content averaged over area A at  $t = 13, 14, 15$ , and  $16$  LST in the cases with and without TICE. It is shown that snow particles comprise the most of cloud mass, followed by graupel particles. In Figure 8, the maximum snow content at  $t = 13$  LST is seen at  $z \sim 10$  km. This implies that a main mechanism for the production and increase of snow mass in this case is the depositional growth of ice crystal and snow particles because the supercooled drop mass is rarely seen at the altitude at this time. At  $t = 13\text{--}14$  LST, the snow mass increases due to TICE, and this increase in snow mass seems to affect the increase in rainwater amount. At  $t = 15$  LST, the snow mass in the case without TICE becomes larger than that in the case with TICE, but it affects little the near-surface rainwater amount because the clouds have been weakened after that time.

To examine the reasons for these changes in snow mass due to TICE, the vertical cross sections (following the black solid line in Figure 6) of relative humidity with respect to ice in the case with TICE and the difference in relative humidity between the cases with and without TICE at  $t = 12, 13$ , and  $14$  LST are shown in Figure 9. At  $t = 12$  LST, there is a sharp boundary between the moist air and the dry air

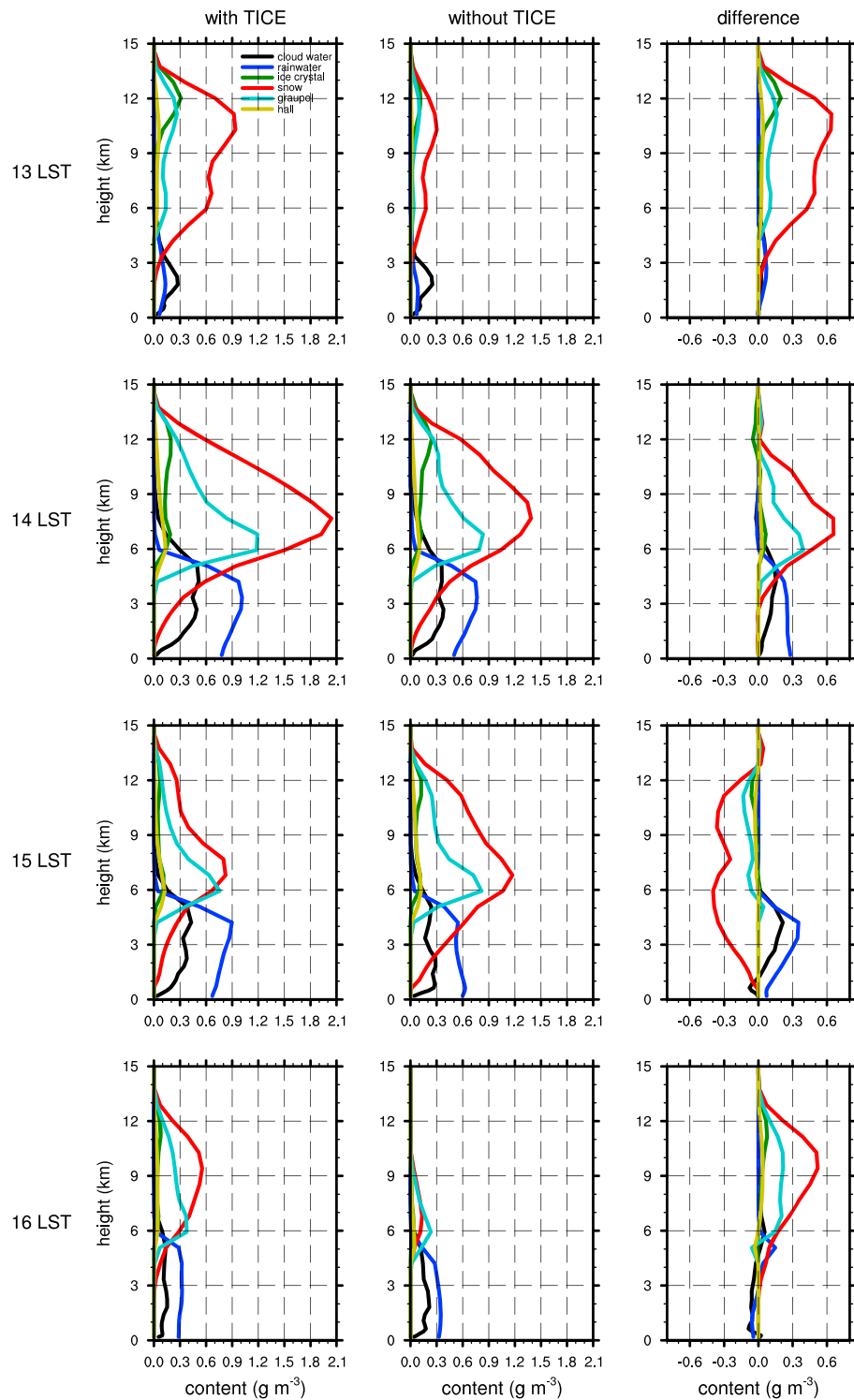


**Figure 8.** Vertical profiles of each hydrometeor content averaged over area A at  $t =$  (from top to bottom, respectively) 13, 14, 15, and 16 LST in the case (left column) with TICE and (middle column) without TICE. (right column) The difference between the cases with and without TICE.

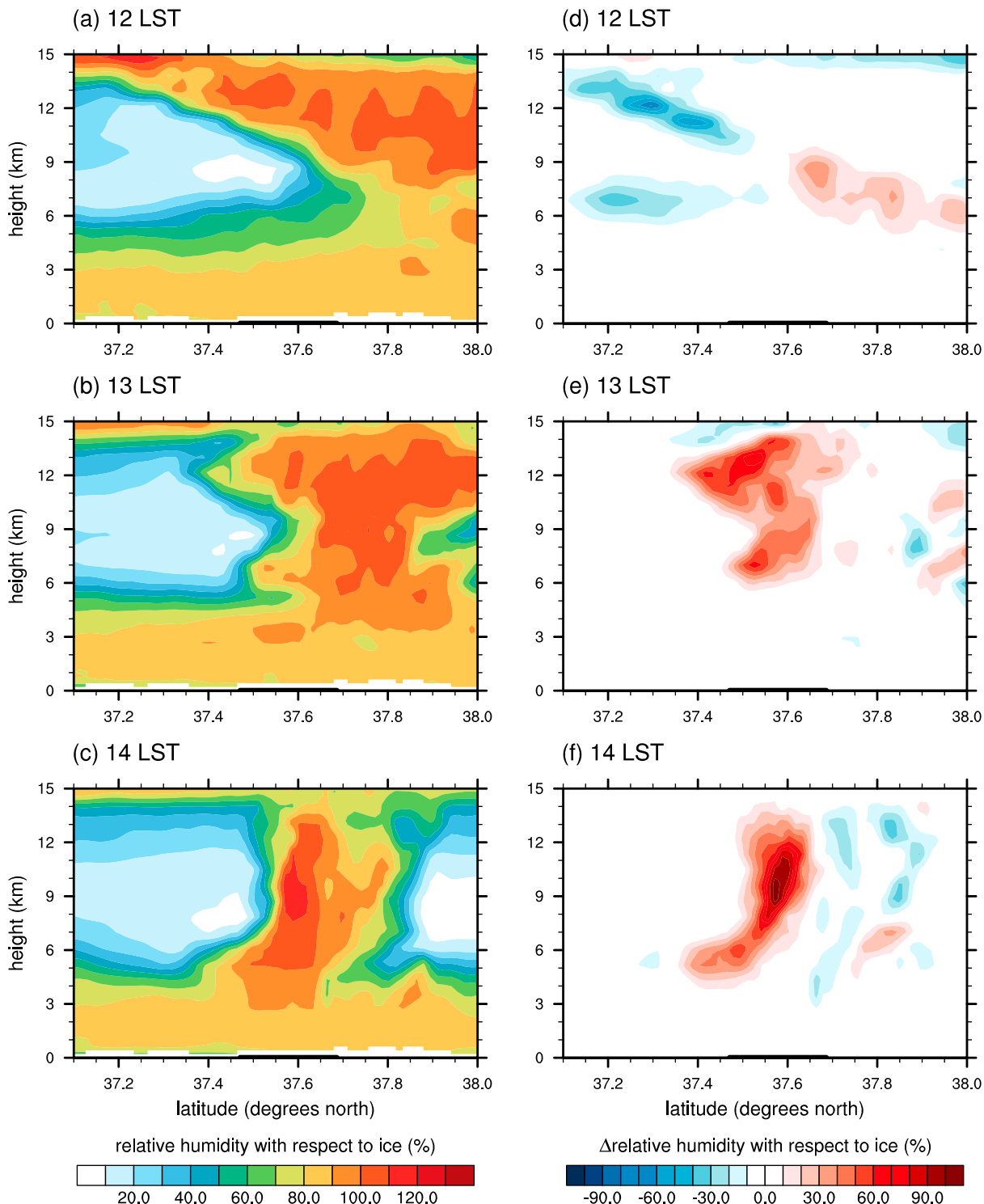


**Figure 9.** Vertical cross sections of relative humidity with respect to ice along the black line in Figure 6 at  $t =$  (a) 12 LST, (b) 13 LST, and (c) 14 LST in the case with TICE. Thick black lines correspond to area A. (d)–(f) The same as Figures 9a–9c but for the difference in relative humidity with respect to ice caused by TICE.

(Figure 9a). In the lower layer of the boundary, relative humidity is higher in the case with TICE than in the case without TICE. At  $t = 13$  LST, the clouds show an upright structure and relative humidity with respect to ice in the clouds is higher in the case with TICE than in the case without TICE because of the increase in water vapor that is transported from the lower layer. Although relative humidity in the

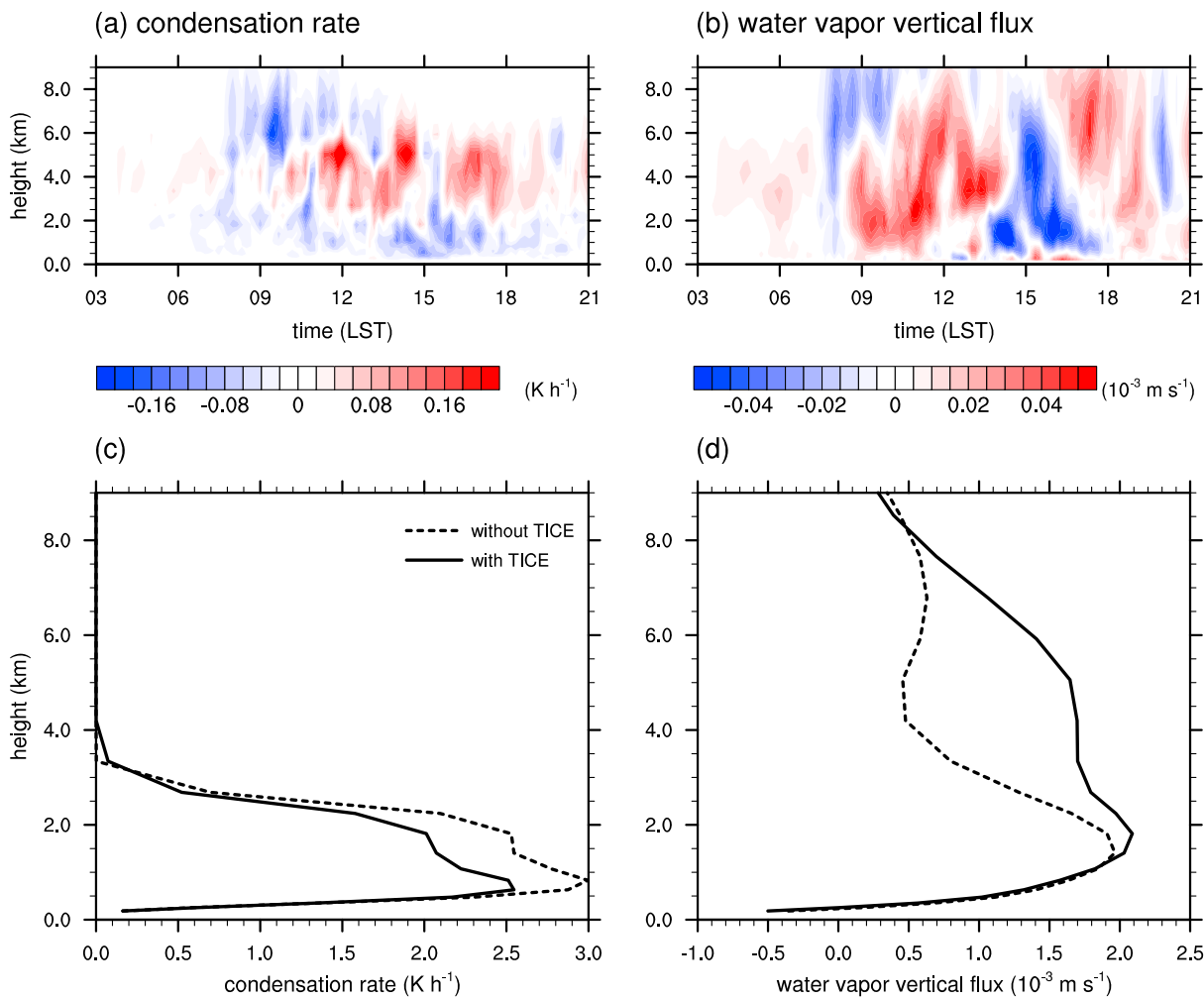
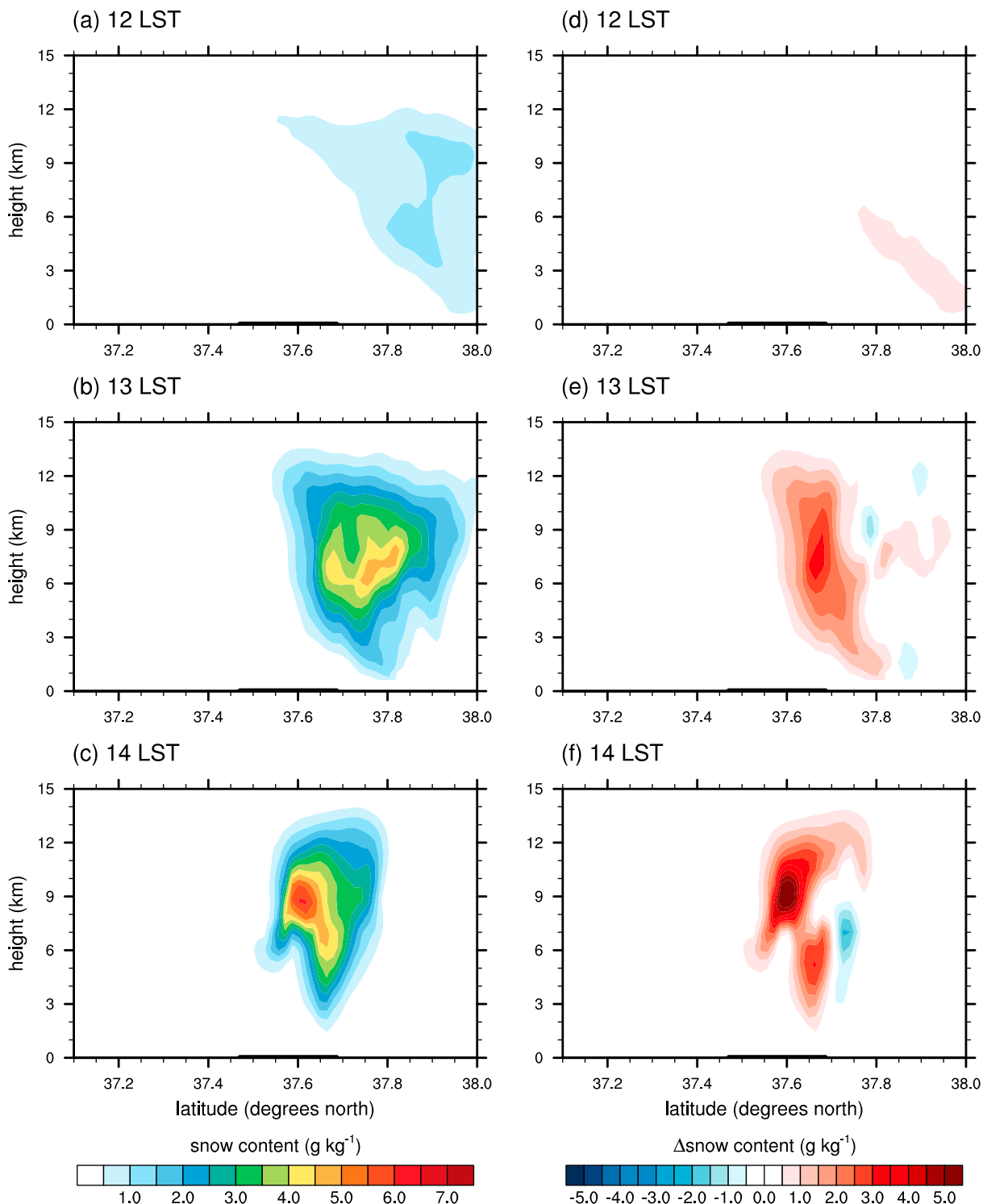


**Figure 10.** Time evolution of horizontally averaged differences in (a) condensation rate and (b) water vapor vertical flux between the cases with and without TICE averaged over the domain, and the vertical profiles of (c) condensation rate and (d) water vapor vertical flux averaged over the area that includes area A and extended to include the cross section shown in Figure 9 for 12–13 LST.

case without TICE becomes higher at  $t = 14$  LST, as the dry air comes from the northwest, the cloudy area becomes narrower.

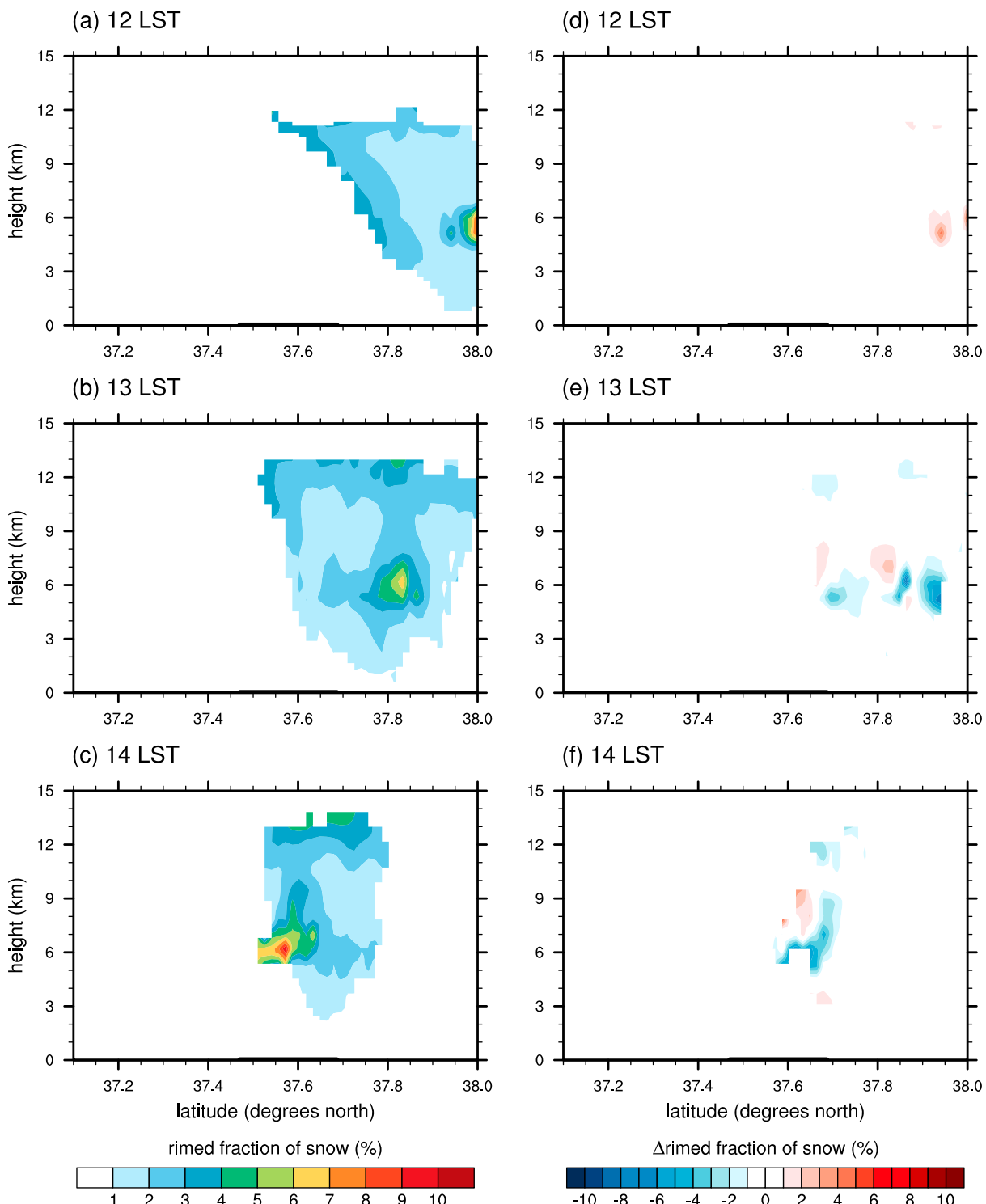
The increase in relative humidity in the lower layer due to TICE at the early cloud development stage similarly appears in Lee *et al.* [2015]. The accelerated coalescence between small cloud droplets due to TICE induces a decrease in the sum of drop surface areas. Because the condensation rate is expressed by the product of drop surface area (proportional to the square of drop radius) and water vapor flux across the drop surface (inversely proportional to drop radius), the decrease in the sum of drop surface areas causes a decrease in condensation. Therefore, more excess water vapor can be transported upward in the case with TICE. Figure 10 shows the time evolutions of differences in horizontally averaged condensation rate and vertical flux of water vapor averaged over the domain, and the vertical profiles of condensation rate and water vapor vertical flux averaged over area A for  $t = 12\text{--}13$  LST. The same changes are observed both in the domain and in area A: the condensation rate in the lower layer ( $z \lesssim 2$  km) is decreased, and the water vapor vertical flux is generally increased due to TICE. These changes can be explained by the accelerated coalescence between small cloud droplets due to TICE.

Figure 11 shows the snow mass distribution on the cross section as in Figure 9. At  $t = 12$  LST, snow starts to be produced mainly near the boundary shown in Figure 9a. The snow mass is larger in the case with TICE than in



**Figure 11.** As in Figure 9 but for snow mass.

the case without TICE mainly due to the increased relative humidity with respect to ice (Figure 9d). The snow mass then can be transported upward more in the case with TICE. At  $t = 13$  and  $14$  LST, the snow mass in the clouds is still larger in the case with TICE than in the case without TICE. The increase in snow mass at high altitudes is largely due to the increased excess water vapor as discussed above (Figures 9 and 10).



**Figure 12.** As in Figure 9 but for the rimed fraction of snow.

Although riming seems to be less important for the increase in snow mass than deposition in this case (Figure 8), it is possible that the growth of snow particles by riming is reduced due to TICE because the accelerated coalescence between small droplets can cause the more sedimentation of large drops and the more reduction of the supercooled drops aloft. In addition, because the rimed snow particle has a larger terminal

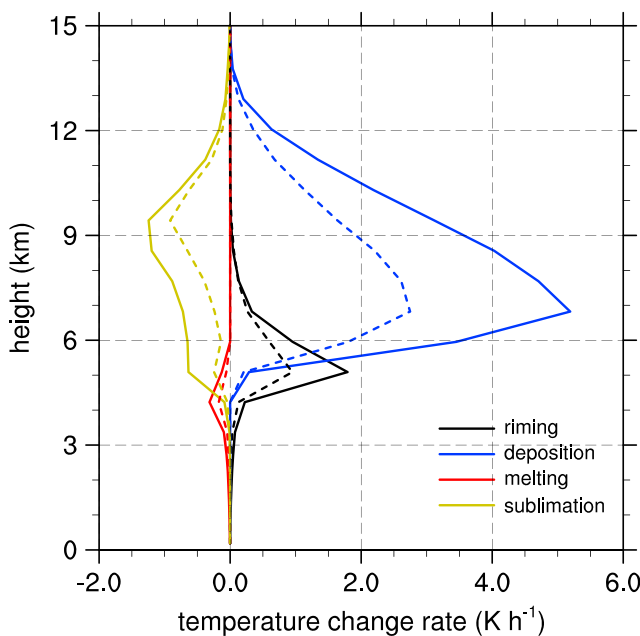


**Figure 13.** Vertical profiles of temperature change rate due to riming, deposition, melting, and sublimation averaged over area A for 12–14 LST in the case with TICE (solid lines) and without TICE (dashed lines).

tion of snow in the clouds due to the reduced droplets aloft at  $t = 13$  and 14 LST, as expected above. However, the large rimed fraction is concentrated only at small part of the clouds, and the value of rimed fraction and the difference in rimed fraction are generally small.

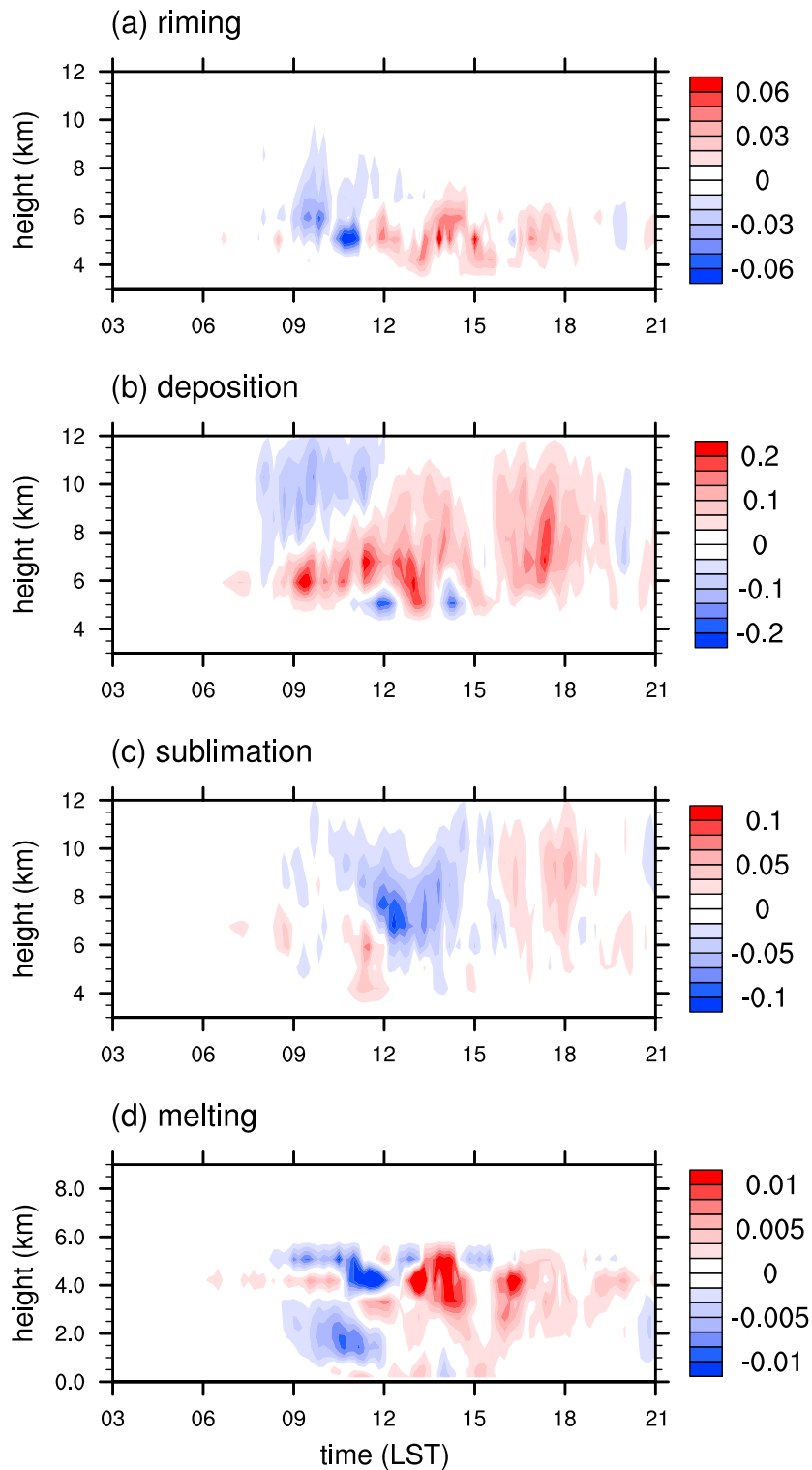
Figure 13 shows the vertical profiles of temperature change rate (i.e., latent heat release rate due to deposition and freezing or latent heat absorption rate due to sublimation and melting) averaged over area A for 12–14 LST. First, an increase in depositional growth due to TICE, which is induced by the increase in upward transport of water vapor (Figure 10d), is observed. In addition, the growth of ice particles due to riming is larger in the case with TICE than in the case without TICE in spite of the decreased rimed fraction of snow due to TICE (Figure 12). This is because TICE increases ice mass by depositional growth so the increase in ice mass due to riming, which is the product of the riming rate per unit ice mass and ice mass, can be also larger in the case with TICE than that in the case without TICE although TICE decreases the rimed fraction. This increase in ice mass induced by TICE causes an increase in melting of ice particles. It is noted that riming is the most dominant process in increasing the ice mass, although the temperature change rate due to deposition is highest. This is because the latent heat rate from vapor to ice per unit mass is approximately 8 times the latent heat rate from water to ice per unit mass, but the temperature change rate due to deposition is only approximately 3 times that due to riming.

Figure 14 shows the same quantities as in Figure 13 but as the time evolution of differences in them between the cases with and without TICE averaged over the entire domain. The important changes in cloud microphysical processes due to TICE that are observed in area A are also observed in the entire domain: deposition, riming, and melting are increased due to TICE. The increase in water vapor vertical flux (Figure 10b) caused by the decrease in condensation rate in the lower layer (Figure 10a) results in the increase in deposition, and the increase in ice mass due to the increased depositional growth results in the increase in riming and melting of ice particles. A series of these microphysical changes due to TICE can cause an increase in surface precipitation in some areas, hence contributing to the spatial shifts in surface precipitation shown in Figure 6.

Figure 15 shows the size distributions of snow at  $z = 4, 7$ , and 10 km at  $t = 13$  LST and 14 LST in the cases with and without TICE. From 13 to 14 LST, the snow mass at  $z = 4$  and 7 km increases, which reflects the

velocity than the pristine snow particle of the same mass, the decreased riming can induce a decrease in snow mass in the lower layer of the clouds by the decrease in the terminal velocity of the snow. However, it is also possible that TICE can increase riming because of the increased snow mass due to depositional growth. In this case, although the riming rate might be smaller, the total amount of riming, which is the product of the riming rate per unit snow mass (or the rimed fraction of snow) and snow mass, can be larger due to the increased snow mass.

Figure 12 shows the rimed fraction of snow on the cross section as in Figure 9 in both cases. First, the rimed fraction of snow generally exhibits a maximum near  $z \sim 6$  km because the number of supercooled drops decreases significantly with increasing altitude. At  $t = 12$  LST, it is shown that TICE does reduce the rimed fraction



**Figure 14.** Time evolution of horizontally averaged differences in (a) riming rate, (b) deposition rate, (c) sublimation rate, and (d) melting rate between the cases with and without TICE averaged over the domain. All units are  $\text{K h}^{-1}$ .

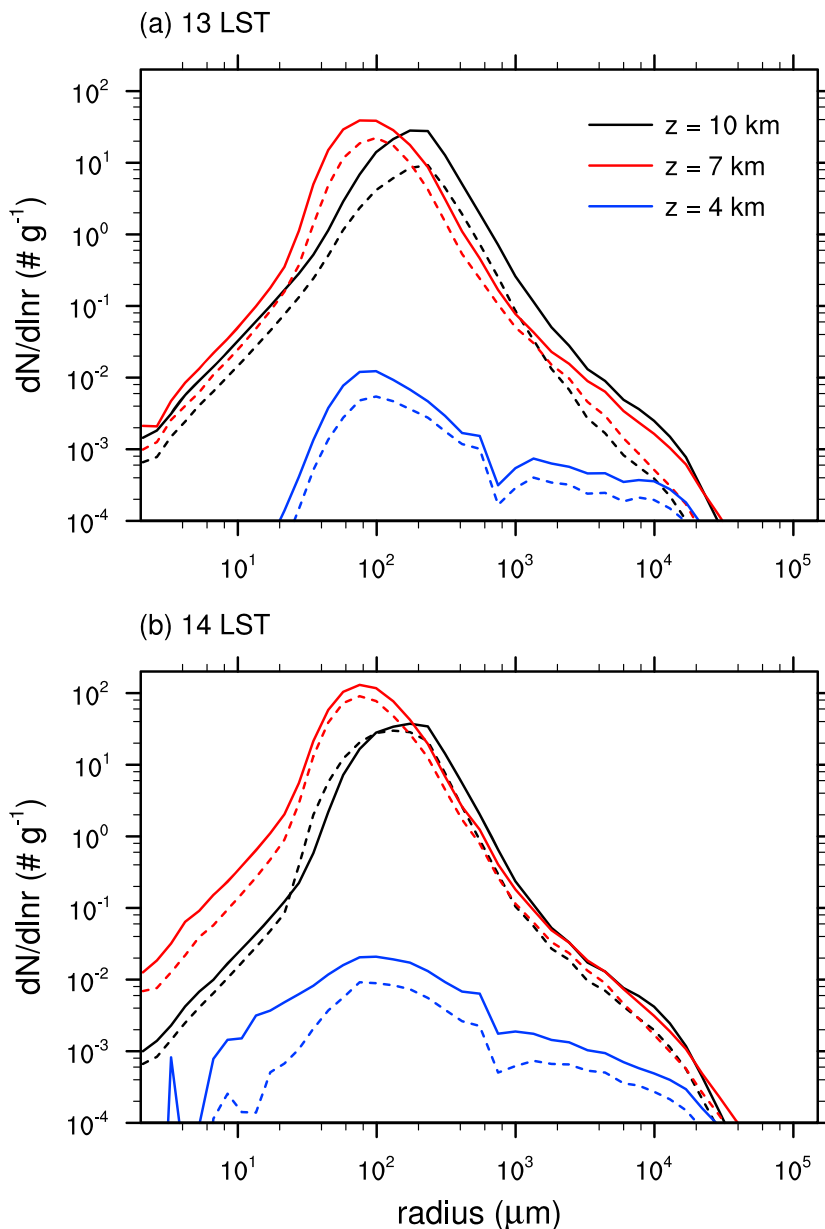


**Figure 15.** Size distributions of snow at  $z = 4, 7$ , and  $10 \text{ km}$  averaged over area A at  $t =$  (a) 13 LST and (b) 14 LST in the case with TICE (solid lines) and without TICE (dashed lines).

sedimentation of snow and the increase in snow mass by riming (Figures 8 and 12). At all altitudes, the maximum number concentration of snow appears near the radius of  $\sim 100 \mu\text{m}$  regardless of TICE, so TICE little changes peak snow radius. Instead, TICE increases the snow number concentration in almost the entire range of snow size. This aspect of change in the snow size distribution is partially due to the very effective riming process across the entire range of snow size, and it is similar to the changes in graupel size distribution due to TICE [Lee *et al.*, 2014]. It is seen in Figure 15 that the intercept parameter of snow size distribution function varies significantly. This suggests that bulk microphysics schemes that represent a snow size distribution using a simple function need to employ at least two moments to represent the snow size distribution more appropriately. It is expected that the results of the bin microphysics scheme with TICE are utilized to improve bulk microphysics schemes.

#### 4. Summary and Conclusions

Using the mesoscale model coupled with the updated bin microphysics scheme, the heavy precipitation event that occurred on 21 September 2010 over the Korean Peninsula was numerically simulated and the effects of turbulence-induced collision enhancement (TICE) on the precipitation event were investigated. This heavy precipitation event was driven by the convergence of warm and cold air and large moisture supply to the convergence zone from the tropical depression. The model tends to underestimate the intensity and duration of the precipitation system in the area with strong band-type precipitation. However, the numerical simulation captures well the important features of the observed surface precipitation and radar reflectivity as well as the synoptic conditions.

While the overall amount of surface precipitation is not significantly altered due to TICE, there are shifts in the spatial distribution of surface precipitation. In the northern part of the domain, precipitation is shifted to northwest, and in the southern part of the domain, the shifts in precipitation are complex. The change in surface precipitation amount averaged over the domain due to TICE is small and similar in terms of scale to that due to the perturbed initial conditions. In Seoul and its nearby area where the largest surface precipitation amount was observed, the averaged surface precipitation amount increases in the case with TICE. However, the effects of different flow realizations also contribute to the increase. Further in-depth studies that carefully distinguish between physical effects of TICE and coincidental effects are needed.

TICE accelerates the coalescence between small droplets, which induces a decrease in condensation in the lower layer and an increase in excess water vapor transported upward. This causes an increase in relative humidity with respect to ice at high altitudes, hence strengthening the depositional growth of ice particles. Therefore, the ice mass in the clouds increases due to TICE, and this increase results in the increase in riming and melting of ice particles. Although rimed fraction of snow is reduced by TICE because of the decreased supercooled drops aloft, the total increased amount of ice mass by riming is enhanced due to TICE because of the increased ice mass via the depositional growth. A series of these cloud microphysical changes are observed both in the entire domain and in Seoul and its nearby area. These changes due to TICE are regarded as partially contributing to the increase in surface precipitation amount in some areas, hence inducing the shifts in the spatial distribution of surface precipitation. Snow size distribution shows that TICE little changes peak snow radius, but the snow number concentration increases in almost the entire radius range.

In this study, similar to other recent numerical studies that use a bin microphysics scheme [e.g., *Fan et al.*, 2014; *Iguchi et al.*, 2014; *Lynn et al.*, 2016], the horizontal grid size of the innermost domain is limited to an order of 1–2 km due to computing resources. The turbulent kinetic energy that needs to calculate the turbulent parameters is provided as a grid-averaged value in the numerical model, whereas the turbulent parameters generally show a high spatial variability [e.g., *Benmoshe et al.*, 2012; *Benmoshe and Khain*, 2014; *Lee et al.*, 2014]. With this limitation, this study should be regarded as a first trial to investigate the small-scale turbulence effects on cloud development and precipitation through real-case simulations. Although the grid size in this study is not very fine, the overall intensity of turbulence simulated in this study is in the range of the results of previous studies which employed a few tens or hundred meters of grid size. However, a finer grid size can resolve turbulence more reliably, and it was reported that the resolved turbulence can alter the midlevel entrainment and cloud development [*Bryan and Morrison*, 2012]. Therefore, although the experiments with finer grid sizes are not realized in this study due to the limited computing resources, high-resolution simulations are needed in future works. Moreover, some recent studies consider the turbulence-induced collision enhancement on collisions between ice crystals [e.g., *Benmoshe and Khain*, 2014; *Siewert et al.*, 2014]. More detailed real-case studies with more rigorous consideration of turbulence effects are needed in future works.

#### Appendix A: Descriptions of Obtaining TKE and Turbulence Parameters

The governing equation of TKE in the Mellor-Yamada-Janjic (MYJ) scheme is given as

$$\frac{dk}{dt} - \frac{\partial}{\partial z} \left( I_1 q S_q \frac{\partial k}{\partial z} \right) = P_s + P_b - \varepsilon, \quad (A1)$$

where  $k$  is TKE,  $I_1$  is the master length scale,  $q=(2k)^{1/2}$ , and  $S_q=0.2$ .  $P_s$ ,  $P_b$ , and  $\varepsilon$  represent the shear production, buoyancy contribution, and turbulence dissipation rate, respectively, which are given as

$$P_s = - \langle uw \rangle \frac{\partial U}{\partial z} - \langle vw \rangle \frac{\partial V}{\partial z}, \quad (\text{A2})$$

$$P_b = \beta g \langle w \theta_v \rangle, \quad (\text{A3})$$

$$\varepsilon = \frac{q^3}{B_1 I_1}, \quad (\text{A4})$$

where  $u$ ,  $v$ , and  $w$  are the perturbation velocity in  $x$ ,  $y$ , and  $z$  directions, respectively, and  $U$  and  $V$  are the mean velocity in  $x$  and  $y$  directions, respectively.  $\beta$  is a constant ( $=1/273$ ),  $g$  is the gravitational acceleration,  $\theta_v$  is the perturbation virtual potential temperature, and  $B_1$  is a constant that is determined from experimental data as discussed in *Janjic* [2002]. After some manipulations introduced in *Janjic* [2002], equation (A1) can be expressed as an ordinary differential equation

$$\frac{d(I_1/q)}{dt} = - \left[ \frac{A(I_1/q)^4 + B(I_1/q)^2}{C(I_1/q)^4 + D(I_1/q)^2 + 1} - \frac{1}{B_1} \right], \quad (\text{A5})$$

where  $A$ ,  $B$ ,  $C$ , and  $D$  are given in equations (3.17)–(3.20) of *Janjic* [2002]. By solving equation (A5) numerically, TKE is obtained both in the free atmosphere and in the boundary layer. In the MYJ scheme, equation (A5) is solved using a two-step iteration method. Moreover, a technique to avoid singularity in solving equation (A5) is introduced in *Janjic* [2002].

Once TKE ( $k$ ) and the buoyancy frequency ( $N$ ) are given, the turbulence dissipation rate and Taylor microscale Reynolds number can be diagnosed following the procedure below. The mixing length  $I_2$  is calculated as [e.g., *Skamarock et al.*, 2008]

$$I_2 = \begin{cases} (\Delta x \Delta y \Delta z)^{1/3}, & \text{if } N^2 \leq 0 \\ \min \left( (\Delta x \Delta y \Delta z)^{1/3}, 0.76 \frac{\sqrt{k}}{N} \right), & \text{if } N^2 > 0 \end{cases} \quad (\text{A6})$$

where  $\Delta x$ ,  $\Delta y$ , and  $\Delta z$  are the grid sizes in  $x$ ,  $y$ , and  $z$  directions, respectively. Then the turbulence dissipation rate  $\varepsilon$  is calculated as

$$\varepsilon = \frac{Ck^{3/2}}{I_2}, \quad (\text{A7})$$

where  $C = 1.9C_k + (0.93 - 1.9C_k)I_2/(\Delta x \Delta y \Delta z)^{1/3}$  and  $C_k = 0.2$ . The root-mean-square velocity fluctuations  $u_{\text{rms}}$  can be evaluated as

$$u_{\text{rms}} = \sqrt{\frac{2}{3} E_{\text{tot}}}. \quad (\text{A8})$$

Here the total turbulent kinetic energy  $E_{\text{tot}}$  is calculated as  $E_{\text{tot}} = (\varepsilon L)^{2/3}$ , where  $L$  is the external turbulence scale. The Taylor microscale length scale  $\lambda$  is calculated as

$$\lambda = u_{\text{rms}} \sqrt{\frac{15\nu}{\varepsilon}}, \quad (\text{A9})$$

where  $\nu$  is the air viscosity. Finally, the Taylor microscale Reynolds number  $\text{Re}_\lambda$  is defined as

$$\text{Re}_\lambda = \frac{u_{\text{rms}} \lambda}{\nu}. \quad (\text{A10})$$

A more detailed description to diagnose the turbulence dissipation rate and Taylor microscale Reynolds number from TKE and buoyancy frequency is given in *Benmoshe et al.* [2012]. For the length scale that is used to diagnose the Taylor microscale Reynolds number, the turbulence mixing length replaces the external turbulence length scale derived from the size of the cloud simulated in the model domain [*Benmoshe et al.*, 2012] in

this study. It might be possible that this alternation causes a slight underestimation of the Taylor microscale Reynolds number due to the decreased length scale. However, the dependency of TICE on the Taylor microscale Reynolds number is generally small [e.g., *Seifert et al.*, 2010], and the orders of magnitudes of the Taylor microscale Reynolds numbers calculated using either the external turbulence length scale or the mixing length are similar to each other [*Benmoshe et al.*, 2012].

### Acknowledgments

The authors are grateful to Wojciech W. Grabowski and two anonymous reviewers for providing valuable comments on this study. All data of this study are accessible via personal communication with the corresponding author (jjbaik@snu.ac.kr). The authors were supported by the National Research Foundation of Korea (NRF) grant funded by the Korea Ministry of Science, ICT and Future Planning (MSIP) (2011-0017041) and also by the Korea Meteorological Administration Research and Development Program under grant KMIPA 2015-5190. The authors thank supercomputer management division of the Korea Meteorological Administration for providing us with the supercomputer resource.

### References

- Ayala, O., B. Rosa, and L.-P. Wang (2008), Effects of turbulence on the geometric collision rate of sedimenting droplets. Part II: Theory and parameterization, *New J. Phys.*, **10**, 075016.
- Benmoshe, N., and A. P. Khain (2014), The effects of turbulence on the microphysics of mixed-phase deep convective clouds investigated with a 2-D cloud model with spectral bin microphysics, *J. Geophys. Res. Atmos.*, **119**, 207–221, doi:10.1002/2013JD020118.
- Benmoshe, N., M. Pinsky, A. Pokrovsky, and A. Khain (2012), Turbulent effects on the microphysics and initiation of warm rain in deep convective clouds: 2-D simulations by a spectral mixed-phase microphysics cloud model, *J. Geophys. Res.*, **117**, D06220, doi:10.1029/2011JD016603.
- Bigg, E. K. (1953), The formation of atmospheric ice crystals by the freezing of droplets, *Q. J. R. Meteorol. Soc.*, **79**, 510–519.
- Bluestein, H. B. (1993), *Synoptic-Dynamic Meteorology in Midlatitudes, vol. II, Observations and Theory of Weather Systems*, 594 pp., Oxford Univ. Press, New York.
- Bryan, G. H., and H. Morrison (2012), Sensitivity of a simulated squall line to horizontal resolution and parameterization of microphysics, *Mon. Weather Rev.*, **140**, 202–225.
- Chen, F., and J. Dudhia (2001), Coupling an advanced land-surface/hydrology model with the Penn State/NCAR MM5 modeling system. Part I: Model description and implementation, *Mon. Weather Rev.*, **129**, 569–585.
- Dudhia, J. (1989), Numerical study of convection observed during the winter monsoon experiment using a mesoscale two-dimensional model, *J. Atmos. Sci.*, **46**, 3077–3107.
- Fan, J., et al. (2014), Aerosol impacts on California winter clouds and precipitation during CalWater 2011: Local pollution versus long-range transported dust, *Atmos. Chem. Phys.*, **14**, 81–101.
- Franklin, C. N. (2008), A warm rain microphysics parameterization that includes the effect of turbulence, *J. Atmos. Sci.*, **65**, 1795–1816.
- Franklin, C. N. (2014), The effects of turbulent collision-coalescence on precipitation formation and precipitation-dynamical feedbacks in simulations of stratocumulus and shallow cumulus convection, *Atmos. Chem. Phys.*, **14**, 6557–6570.
- Franklin, C. N., P. A. Vaillancourt, M. K. Yau, and P. Bartello (2005), Collision rates of cloud droplets in turbulent flows, *J. Atmos. Sci.*, **62**, 2451–2466.
- Grabowski, W. W. (2014), Extracting microphysical impacts in large-eddy simulations of shallow convection, *J. Atmos. Sci.*, **71**, 4493–4499.
- Grabowski, W. W. (2015), Untangling microphysical impacts on deep convection applying a novel modeling methodology, *J. Atmos. Sci.*, **72**, 2446–2464.
- Grabowski, W. W., and L.-P. Wang (2013), Growth of cloud droplets in a turbulent environment, *Annu. Rev. Fluid Mech.*, **45**, 293–324.
- Grabowski, W. W., L.-P. Wang, and T. V. Prabha (2015), Macroscopic impacts of cloud and precipitation processes on maritime shallow convection as simulated by a large eddy simulation model with bin microphysics, *Atmos. Chem. Phys.*, **15**, 913–926.
- Hallett, J., and S. C. Mossop (1974), Production of secondary ice crystals during the riming process, *Nature*, **249**, 26–28.
- Huffman, G. J., D. T. Bolvin, E. J. Nelkin, D. B. Wolff, R. F. Adler, G. Gu, Y. Hong, K. P. Bowman, and E. F. Stocker (2007), The TRMM multisatellite precipitation analysis (TMPA): Quasi-global, multiyear, combined-sensor precipitation estimates at fine scales, *J. Hydrometeorol.*, **8**, 38–55.
- Iguchi, T., T. Matsui, W.-K. Tao, A. P. Khain, V. T. J. Phillips, C. Kidd, T. L'Ecuyer, S. A. Braun, and A. Hou (2014), WRF-SBM simulations of melting-layer structure in mixed-phase precipitation events observed during LPVEx, *J. Appl. Meteorol. Climatol.*, **53**, 2710–2731.
- Janjic, Z. I. (2002), Nonsingular implementation of the Mellor-Yamada Level 2.5 scheme in the NCEP Meso model, NCEP Office Note, No. 437, 61 pp.
- Jiang, B., B. Huang, W. Lin, and S. Xu (2016), Investigation of the effects of anthropogenic pollution on typhoon precipitation and microphysical processes using WRF-Chem, *J. Atmos. Sci.*, **73**, 1593–1620.
- Jiang, Q., and S. Wang (2014), Aerosol replenishment and cloud morphology: A VOCALS example, *J. Atmos. Sci.*, **71**, 300–311.
- Jung, W., and T.-Y. Lee (2013), Formation and evolution of mesoscale convective systems that brought the heavy rainfall over Seoul on September 21, 2010, *Asia Pac. J. Atmos. Sci.*, **49**, 635–647.
- Kain, J. S. (2004), The Kain-Fritsch convective parameterization: An update, *J. Appl. Meteorol.*, **43**, 170–181.
- Khain, A., M. Ovtchinnikov, M. Pinsky, A. Pokrovsky, and H. Krugliak (2000), Notes on the state-of-the-art numerical modeling of cloud microphysics, *Atmos. Res.*, **55**, 159–224.
- Khain, A., D. Rosenfeld, A. Pokrovsky, U. Blahak, and A. Ryzhkov (2011), The role of CCN in precipitation and hail in a mid-latitude storm as seen in simulations using a spectral (bin) microphysics model in a 2D dynamic frame, *Atmos. Res.*, **99**, 129–146.
- Köhler, H. (1936), The nucleus in and the growth of hygroscopic droplets, *Trans. Faraday Soc.*, **32**, 1152–1161.
- Kunnen, R. P. J., C. Siewert, M. Meinke, W. Schröder, and K. D. Beheng (2013), Numerically determined geometric collision kernels in spatially evolving isotropic turbulence relevant for droplets in clouds, *Atmos. Res.*, **127**, 8–21.
- Lee, H., J.-J. Baik, and J.-Y. Han (2014), Effects of turbulence on mixed-phase deep convective clouds under different basic-state winds and aerosol concentrations, *J. Geophys. Res. Atmos.*, **119**, 13,506–13,525, doi:10.1002/2014JD022363.
- Lee, H., J.-J. Baik, and J.-Y. Han (2015), Effects of turbulence on warm clouds and precipitation with various aerosol concentrations, *Atmos. Res.*, **153**, 19–33.
- Lynn, B. H., A. P. Khain, J. W. Bao, S. A. Michelson, T. Yuan, G. Kelman, D. Rosenfeld, J. Shpund, and N. Benmoshe (2016), The sensitivity of Hurricane Irene to aerosols and ocean coupling: Simulations with WRF spectral bin microphysics, *J. Atmos. Sci.*, **73**, 467–486.
- Meyers, M. P., P. J. DeMott, and W. R. Cotton (1992), New primary ice-nucleation parameterizations in an explicit cloud model, *J. Appl. Meteorol.*, **31**, 708–721.
- Mlawer, E. J., S. J. Taubman, P. D. Brown, M. J. Iacono, and S. A. Clough (1997), Radiative transfer for inhomogeneous atmosphere: RRTM, a validated correlated-k model for the long-wave, *J. Geophys. Res.*, **102**, 16,663–16,682, doi:10.1029/97JD00237.
- Phillips, V. T. J., A. Pokrovsky, and A. Khain (2007), The influence of time-dependent melting on the dynamics and precipitation production in maritime and continental storm clouds, *J. Atmos. Sci.*, **64**, 338–359.

- Pinsky, M., A. Khain, D. Rosenfeld, and A. Pokrovsky (1998), Comparison of collision velocity differences of drops and graupel particles in a very turbulent cloud, *Atmos. Res.*, 49, 99–113.
- Pinsky, M., A. Khain, and H. Krugliak (2008), Collisions of cloud droplets in a turbulent flow. Part V: Application of detailed tables of turbulent collision rate enhancement to simulation of droplet spectra evolution, *J. Atmos. Sci.*, 65, 357–374.
- Saffman, P. G., and J. S. Turner (1956), On the collision of drops in turbulent clouds, *J. Fluid Mech.*, 1, 16–30.
- Seifert, A., L. Nuijens, and B. Stevens (2010), Turbulence effects on warm-rain autoconversion in precipitating shallow convection, *Q. J. R. Meteorol. Soc.*, 136, 1753–1762.
- Siewert, C., R. P. J. Kunnen, and W. Schröder (2014), Collision rates of small ellipsoids settling in turbulence, *J. Fluid Mech.*, 758, 686–701.
- Skamarock, W. C., et al. (2008), A description of the Advanced Research WRF version 3, NCAR Tech. Note NCAR/TN-475+STR, 113 pp.
- Twomey, S. (1959), The nuclei of natural cloud formation. Part II: The supersaturation in natural clouds and the variation of cloud droplet concentration, *Pure Appl. Geophys.*, 43, 243–249.
- Vali, G. (1975), Remarks on the mechanism of atmospheric ice nucleation, in *Proceedings of the 8th International Conference on Nucleation*, pp. 265–269, Gidrometeoizdat, Saint Petersburg.
- Wang, L.-P., O. Ayala, B. Rosa, and W. W. Grabowski (2008), Turbulent collision efficiency of heavy particles relevant to cloud droplets, *New J. Phys.*, 10, 075013.
- Wyszogrodzki, A. A., W. W. Grabowski, L.-P. Wang, and O. Ayala (2013), Turbulent collision-coalescence in maritime shallow convection, *Atmos. Chem. Phys.*, 13, 8471–8487.
- Zhou, Y., A. S. Wexler, and L.-P. Wang (2001), Modelling turbulent collision of bidisperse inertial particles, *J. Fluid Mech.*, 433, 77–104.